

## Time dependence of intraplate volcanism caused by shear-driven upwelling of low-viscosity regions within the asthenosphere

Todd Anthony Bianco,<sup>1,2</sup> Clinton P. Conrad,<sup>2</sup> and Eugene I. Smith<sup>3</sup>

Received 28 January 2011; revised 7 July 2011; accepted 11 September 2011; published 18 November 2011.

[1] Although volcanism far from tectonic boundaries is likely due to upwelling near the lithospheric base, the convective processes that induce upwelling are unclear. Numerical models show that asthenospheric shear can be deflected upward by lateral viscosity variations within the asthenosphere, producing “shear-driven upwelling” (SDU). To constrain the rate, duration, and surface expression of intraplate volcanism caused by SDU, we simulate 2-D flow and peridotite melting in the upper 200 km of the mantle. Asthenospheric shear is driven by lithospheric plates with different thicknesses moving at 3–9 cm/yr, and the initial low-viscosity region is a rectangularly shaped pocket with an imposed viscosity that is 2 orders of magnitude smaller than the surrounding asthenosphere. Melting decreases as the pocket deforms and reaches steady state after 3–12 Myr. The age progression of surface volcanism is nearly stationary in the reference frame of the plate, which distinguishes SDU from hot spot volcanism. Similar behavior occurs if the viscosity heterogeneity is induced by variations in the water content of mantle peridotite. If the pocket’s low viscosity is caused by excess temperature, buoyant upwelling of the entire pocket dominates volcanism. Differences in the time dependence of volcanism associated with damp and warm pockets may help identify which type of mantle heterogeneity and associated dynamic process best explains weak, intermittent, intraplate volcanism with no obvious age progression. We suggest that asthenospheric shear induced by plate motions and global mantle flow, by exciting SDU, drives some of the non-hot spot small-scale volcanism that occurs away from plate boundaries.

**Citation:** Bianco, T. A., C. P. Conrad, and E. I. Smith (2011), Time dependence of intraplate volcanism caused by shear-driven upwelling of low-viscosity regions within the asthenosphere, *J. Geophys. Res.*, 116, B11103, doi:10.1029/2011JB008270.

### 1. Introduction

[2] Although there are many examples of intraplate volcanism on Earth’s continents and ocean floor, the origin of much of this volcanism is not well explained. Currently, the most successful explanation for the formation of intraplate volcanism is the thermal plume hypothesis, by which warm, buoyant material rises from some depth in the mantle, and the excess temperature of the plume allows for melting away from plate boundaries [Wilson, 1963; Morgan, 1971, 1972]. The plume hypothesis makes a number of predictions, such as the existence of flood basalts formed by the plume head [Morgan, 1971; Whitehead and Luther, 1975; Richards *et al.*, 1989], the eruption of a “hot spot” trail of volcanoes with an age progression formed by plate motion, topographic swells

caused by the density contrast of the plume material [Olson and Nam, 1986; Davies, 1988; Sleep, 1990], seismically slow anomalies caused by the temperature contrast of plume material [e.g., Anderson, 1989; Hirth and Kohlstedt, 1996, 2003], and compositional differences among hot spot volcanoes generated by plume material of different temperatures, pressures, and sources [e.g., Allègre, 1982; Zindler and Hart, 1986; Hofmann, 1997].

[3] Of the thousands of confirmed examples of intraplate volcanism across the globe and in the geological record, the number that are clearly the result of thermal, plumelike anomalies is on the order of tens, and these tend to be the most voluminous examples of intraplate magmatism [Courtillot *et al.*, 2003; Ito and van Keken, 2007]. Of course, there is a lack of data in many instances to rule out a plume source, but many well-studied island chains lack one or more of the major features predicted by the plume hypothesis [Courtillot *et al.*, 2003]. One of the most compelling reasons to reject a plume source for intraplate volcanism is the lack of an obvious hot spot age progression in the spatial-temporal pattern of eruptions. Examples of intraplate volcanism without an age progression consistent with plate motion over a fixed plume include the Line Islands, Marshall Islands, and

<sup>1</sup>Department of Geological Sciences, Brown University, Providence, Rhode Island, USA.

<sup>2</sup>Department of Geology and Geophysics, University of Hawaii at Manoa, Honolulu, Hawaii, USA.

<sup>3</sup>Department of Geoscience, University of Nevada, Las Vegas, Nevada, USA.

Cameroon Line, and even more classical examples such as Samoa and the Puka-Puka ridge have less-than-perfect age progressions throughout their durations [Ito and van Keken, 2007]. Further, no obvious age progression or hot spot track exists in the many Plio-Pleistocene eruptions of the South-western Nevada Volcanic Field [e.g., Smith et al., 2002; Valentine et al., 2006; Valentine and Hirano, 2010] or in some of the volcanism of eastern Australia, particularly in the Newer Volcanic Province in Victoria [e.g., Demidjuk et al., 2007; Gray and McDougall, 2009]. Thus, while plumes may be the cause of some intraplate volcanism, there are numerous examples that may be better explained by some other process.

[4] Many nonplume hypotheses have addressed the lack of an obvious age progression at a hot spot by proposing that the dynamic cause of melt production is a lithospheric process or feature. Examples include small-scale convection such as Richter rolls or other gravitational instabilities [e.g., Buck and Parmentier, 1986; Marquart, 2001; Ballmer et al., 2007; Elkins-Tanton, 2007], plate flexure [Hirano et al., 2006], and extension leading to cracking [Turcotte and Oxburgh, 1978; Sandwell et al., 1995] or upwelling [McKenzie and Bickle, 1988], buoyant melting instabilities [Raddick et al., 2002; Hernlund et al., 2008a, 2008b], and edge-driven flow where the thickness of the lithosphere changes rapidly, such as at craton edges [King and Anderson, 1998; King and Ritsema, 2000; Till et al., 2010]. Further, a small, isolated warm pocket beneath the lithosphere should not exhibit a hot spot trail [Huppert, 1982; Bercovici and Lin, 1996]. A challenge for all of these nonplume hypotheses is predicting large enough eruption rates over long enough time scales to explain observations, which many of the above studies achieved with varying degrees of success.

[5] Recent work has proposed a new process by which asthenospheric shear, generated by relative motion between the surface plates and the underlying mantle flow, is deflected vertically by lateral viscosity variations [Conrad et al., 2010]. This upwelling, which is not driven by local density heterogeneity, is a potential cause for decompression and melting. Conrad et al. [2010] proposed two types of shear-driven upwelling (SDU) associated with two types of lateral viscosity variations: changes in the depth of the lithosphere-asthenosphere boundary (“cavities” or “steps”) and regions of anomalously low-viscosity material embedded within the asthenosphere (“pockets”). As in some previously proposed hypotheses, SDU-induced melting requires decompression of asthenosphere that is already near its solidus. Conrad et al. [2010] treated this near-solidus material as a residual mantle layer [Langmuir et al., 1992] that has not significantly cooled. While Conrad et al. [2010] did estimate rates for volcanism that might be associated with SDU, they did not specifically demonstrate how SDU causes melting, nor address how this melt might be erupted to the surface. Recently, several studies have proposed that SDU-like mechanisms may alter the lithospheric stress field to allow eruption of shear-aligned, melt-rich regions in the upper mantle [Kawakatsu et al., 2009; Kohlstedt and Holtzman, 2009; Anderson, 2010; Holtzman et al., 2003]. Although Conrad et al. [2010] suggested that SDU can create these melt-rich regions, they did not examine the time-dependent

nature of SDU-induced melt production or its volcanic surface expression. Such time-dependent constraints are essential in order to evaluate the viability of SDU as a generator of intraplate volcanism, and to make quantitative predictions about SDU age progression that can be compared against observations. Testing the persistence of SDU is particularly important because Conrad et al. [2010] assumed only rectangular-shaped pockets, which may not be representative of actual asthenospheric heterogeneity (although some tomographic studies show that heterogeneity can be boxy in cross section [e.g., Gao et al., 2004; West et al., 2004]), particularly because pocket shape must be continuously changing when exposed to asthenospheric shear.

[6] Here we present 2-D, time-dependent models of SDU for the second type of lateral viscosity variation examined by Conrad et al. [2010]: low-viscosity pockets embedded within a shearing asthenospheric layer. These simulations simultaneously solve for viscous flow patterns and melting of a peridotite source. We predict the rate of melting and volcanic emplacement of melt at the surface, the duration of volcanism, and the spatial and temporal patterns of eruption. We determine which parameters, such as the dimensions of pockets, the thickness of plates, and the magnitude of shear, control the time dependence of SDU. To explore these parameters, we start simply by examining pockets in which low viscosity is simply imposed (i.e., with no specific natural explanation). Next we examine more realistic causes of low viscosity within these pockets, specifically variations in water content [e.g., Michael, 1988; Dixon et al., 2002, 2004; Asimow and Langmuir, 2003] or temperature. Finally, we compare this robust description of time-dependent SDU melting simulations to observations of intraplate volcanism on continents and the seafloor.

## 2. Methods

### 2.1. Dynamics and Melting

[7] We use the Cartesian finite element code CITCOM to solve for 2-D convection in the upper 200 km of the mantle (i.e., the lithosphere and asthenosphere) [Moresi and Gurnis, 1996; Zhong et al., 2000; van Hunen et al., 2005]. Although CITCOM has been widely used for studies of mantle convection and melting [e.g., Ballmer et al., 2007, 2009; Bianco et al., 2008], we will review the major components of our modeling procedure here.

[8] Our numerical model solves the mass conservation, momentum, energy, and continuity equations for an incompressible, infinite-Prandtl-number fluid. Making the extended Boussinesq approximation, the dimensionless continuity and momentum equations reduce to

$$\nabla \cdot \mathbf{u} = 0 \quad (1)$$

$$-\nabla P + \nabla \cdot [\eta(\nabla \mathbf{u} + \nabla^T \mathbf{u})] + RaT\hat{\mathbf{k}} = 0, \quad (2)$$

where  $\mathbf{u}$  is the velocity vector,  $P$  is pressure,  $\eta$  is dynamic viscosity,  $Ra$  is Rayleigh number (which is unimportant in our simulations in the absence of lateral temperature variations),  $T$  is absolute temperature,  $\hat{\mathbf{k}}$  is vertical unit vector, and all

variables and operators are nondimensional. The dimensionless energy equation is

$$\frac{DT}{Dt} = \nabla^2 T - Q(\mathbf{u}, \dot{M}), \quad (3)$$

where  $DT/Dt$  is the full material time derivative and  $\dot{M}$  is the melting rate. The source term  $Q$  accounts for cooling due to the latent heat of melting and adiabatic decompression. Although viscous dissipation is omitted, other simulations that include this effect show only a small increase in volcanism (M. Ballmer, personal communication, 2008). In nondimensional form,  $Q$  is

$$Q = Di \cdot T \left[ w - \left( \frac{\Delta S}{Di \cdot c_p} \right) \frac{DF}{Dt} \right], \quad (4)$$

where  $Di$  is dissipation number,  $w$  is vertical velocity,  $\Delta S$  is the change in entropy associated with the liquid–solid phase change,  $c_p$  is specific heat, and  $F$  is melt fraction [Christensen and Yuen, 1985].

[9] The width of our model space is 1400 km in most simulations, though some simulations are as wide as 2800 km to avoid boundary effects at the edges, and the depth is 200 km. The side boundaries are open to material flow and have zero conductive heat flow [Ribe and Christensen, 1999]. Both velocity and conductive heat flow are zero at the base of the model. The top surface has an imposed horizontal velocity,  $V_{\text{plate}}$  (and zero vertical velocity) to simulate plate motion, which causes shearing in the asthenosphere below. Vertical and horizontal resolution is uniformly 1.5625 km in all simulations discussed in this paper.

[10] The temperatures of the surface and model base are 25°C and 1482°C, respectively, and the initial condition includes an adiabatic gradient defined as

$$\gamma = \exp(Di \cdot z) - 1, \quad (5)$$

where  $z$  is nondimensional depth, increasing downward. In all simulations, dissipation number,  $Di = 0.0784$  and potential temperature  $T_p = 1350^\circ\text{C}$ , an estimation in the mid-range of values considered by other studies addressing mid-ocean ridges (e.g., 1240°–1475°C [Asimow et al., 2001; Presnall et al., 2002; Putirka, 2005]) and at the lower end of studies addressing continental magmatism in the Western U.S. (e.g., 1350°–1700°C [Wang et al., 2002; Lee et al., 2009]). Notably, these conditions result in ~6 km of crust in our simulations of passively spreading plates, which is consistent with global averages [White et al., 1992; Dick et al., 2003]. We assume a half-space cooling model [Davis and Lister, 1974] and, in most simulations, that the thermal age of the lithosphere is <0.1 Myr so that most of the model space has not cooled by upward diffusion of heat. Thus, we are usually examining the end-member case essentially without an overlying thermal boundary layer, which allows us to predict the maximum amount of melting that may be caused by SDU. To examine the influence of plate thickness on SDU, we impose a mechanical lithosphere (described below) instead of a thermal lithosphere.

[11] We compute the melting and tracking of mantle material using a passive tracer advection scheme [van Hunen et al., 2005]. In every time step, the equilibrium extent of melting ( $F_{\text{eq}}$ ) is calculated using a parameterized

equation for peridotite equilibrium that depends on the local value of  $T$ ,  $P$ , and water content [Katz et al., 2003] at each node. Next, total extent of partial melting from the previous time step ( $F_0$ ) is interpolated from the tracers to the nodes. The new total extent of partial melting at the node ( $F_1$ ) is the maximum of [ $F_0$ ,  $F_{\text{eq}}$ ] and the rate of melting is the maximum of [ $(F_1 - F_0)/dt$ , 0]. Finally,  $F_1$  is interpolated from the nodes back to the tracers, and tracers are advected in the next time step. To calculate rates and volumes of volcanism at the surface, we assume that all melt rises instantly and vertically and spreads over a lateral length equal to the spacing of the nodes (e.g., the width of finite elements), which is consistent with the most simple model of fractional melting. Because we assume that all of the melt escapes, we do not consider refreezing, nor whether  $F$  may be limited by any factor beyond those associated with mantle conditions.

[12] Each simulation is initialized with the assumption that all material has previously risen passively to its current depth. Thus, initially  $F_0 > 0$  in the shallow mantle (~70 km in most simulations), and this represents a residual mantle layer that has formed by passive upwelling beneath a mid-ocean ridge [Langmuir et al., 1992]. In our simulations most of this layer has not cooled by thermal diffusion upward so that the material is at its solidus and will begin melting if it is decompressed. The model best describes the state of young oceanic asthenosphere, as the growth and composition of the continental lithosphere may be more complicated. Beneath continents, near-solidus material similar to what we model in the residual mantle layer may only exist in regions of recent continental extension. Further, continental lithosphere may insulate the mantle below [Gurnis, 1988], which may create conditions that improve the likelihood of melting, but that are different from those modeled here using thermal or mechanical lithospheres. Nevertheless, continental asthenosphere may be near-solidus owing to elevated water content (possibly added by subduction), elevated potential temperature (by excessive radioactive heating or plume material), or some other factor. Our models will show how SDU may cause melting in any of these cases and thus is applicable to both oceanic and continental lithosphere.

## 2.2. Rheology and Viscosity Heterogeneities

[13] All simulations employ viscosity that is controlled by a temperature-dependent, Newtonian rheological law such that

$$\eta = v \exp \left[ \frac{E_a}{R} \left( \frac{1}{T} - \frac{1}{T_r} \right) \right], \quad (6)$$

where  $v$  is a nondimensional premultiplier,  $E_a$  is activation energy,  $R$  is the gas constant, and  $T_r$  is reference temperature [Zhong and Watts, 2002]. A mechanical lithosphere is included in some simulations by setting  $v = 1000$  from the surface to a given depth. Significant upwelling and melting does not occur within the mechanical plate.

[14] Pockets are initialized with relatively low viscosity in one of three ways: by arbitrarily imposing a low-viscosity region (“imposed pocket”), by initializing a region with greater water content than the surrounding asthenosphere (“damp pocket”) or excess temperature (“warm pocket”). The first two types of pockets rely on the tracer-advection scheme described below. The third type, a warm pocket, is

introduced by the initial temperature condition simply by adding a thermal anomaly within the desired area of the pocket; it is then advected by the flow according to (3). The dimensionless height of a pocket,  $H_{LV}$ , is the dimensional height of the pocket divided by the height of the asthenosphere,  $H_{Asth}$ . The dimensionless width of a pocket,  $W_{LV}$ , is defined in the same manner, and pocket's aspect ratio is  $W_{LV}/H_{LV}$ .

[15] In the case of an imposed pocket, our tracer-advection scheme interpolates the premultiplier,  $v$ , from the tracers to the nodes between advection steps. Once this information is at the nodal level, CITCOM can correctly include the viscosity heterogeneity. We initialize tracers inside the pocket with  $v = 0.01$  and outside the pocket with  $v = 1.0$ . We refer to this low-viscosity heterogeneity as an imposed pocket, as we have imposed a drop in viscosity that is not related to any particular physical variation in the asthenosphere.

[16] In the case of a damp pocket,  $v$  must be calculated at the nodal level from other information. We assume that water behaves like an incompatible trace element and is partitioned between solid and melt by modal, fractional melting such that

$$C_s^{H_2O} = C_o^{H_2O}(1 - F)^{1/D-1}, \quad (7)$$

where  $C_s^{H_2O}$  is the concentration of water in the solid residue,  $C_o^{H_2O}$  is the initial concentration, and  $D$  is the bulk partition coefficient. We compute the premultiplier as

$$v = \min \left[ \left( \frac{C_s^{H_2O}}{C_P^{H_2O}} \right)^r, 100 \right]. \quad (8)$$

Here,  $C_s^{H_2O}$  is the concentration of water in the solid residue either inside or outside of the pocket,  $C_P^{H_2O}$  is the initial concentration inside the pocket, and we assume the exponent  $r = -1$  [Hirth, 2002; Hirth and Kohlstedt, 2003]. We interpolate  $C_o^{H_2O}$  from the tracers to the nodes between advection steps, and compute (7) and (8) at the node level. In the simulations below,  $C_P^{H_2O} = 400$  ppm (i.e.,  $C_o^{H_2O}$  inside the pocket), and  $C_o^{H_2O} = 0$  outside the pocket. The 2 orders of magnitude decrease in viscosity between hydrous peridotite with 400 ppm water and anhydrous peridotite captures rheological observations from laboratory experiments [Chopra and Paterson, 1984; Karato et al., 1986; Borch and Green, 1989; Mei and Kohlstedt, 2000; Jung and Karato, 2001].

### 3. Simulations With Imposed Viscosity Heterogeneity

[17] We first discuss simulations of SDU in which we impose viscosity heterogeneity. We thus initially ignore the (hydrous or thermal) cause of the viscosity heterogeneity, which allows us to examine the time dependence of SDU generally before examining the specific effects of water or temperature.

#### 3.1. Patterns of Shear-Driven Upwelling

[18] To demonstrate the flow and melting patterns that arise from SDU, we first consider four example cases of lateral viscosity variations exposed to viscous shear (Figure 1). In an isoviscous scenario, vertical velocity everywhere is zero, and

material moving to the right is replaced by material from the left. However, if the shear flow encounters a “wall”-shaped viscosity decrease (a step function decrease of 2 orders of magnitude in viscosity), then the viscosity heterogeneity can induce a component of vertical flow (Figure 1b). In particular, we find that the lower-viscosity material moving to the right is most easily replaced by low-viscosity material from below, rather than by the higher-viscosity material upstream. Thus, we find plane Couette flow (and zero vertical velocity) far from the viscosity transition, but upwelling vertical velocity on the low-viscosity side of the viscosity transition (Figure 1a). We also find that upwelling occurring downstream of the viscosity transition is fed by material coming from the left, which induces a large downward velocity along, and on both sides of, the viscosity wall (Figure 1a).

[19] In a second example, we isolate the low-viscosity material to a 320 km wide rectangular pocket (Figure 1c). The vertical velocity profile across this transition is similar to the wall case (Figure 1a), but the upwellings on both sides of the pocket edge are amplified compared to the wall case, and the downwelling at the pocket wall is diminished because the height of the pocket is limited. The upwelling is enhanced because of circulation that is induced within the pocket by the shear flow. This circulation, which was described by Conrad et al. [2010], occurs because shear becomes concentrated within the center of the low-viscosity pocket, and upwelling on the upstream side of the pocket is required to feed the faster velocity along the top of the pocket (Figure 1c). The vertical velocity profile is reflected and inverted about the center of the pocket, thus inducing downwelling both inside and outside of the downstream side of the pocket, and local upwelling along the downstream pocket wall.

[20] For alternative pocket shapes of similar dimension, we observe the same basic pattern of upwelling and downwelling. If the walls of the pocket are semicircular (Figure 1d) rather than vertical, the vertical velocity pattern is similar to the rectangular pocket (Figure 1c), although the vertical velocity amplitudes are reduced by ~50% (Figure 1a). Similarly, a pocket with “right-leaning walls” (Figure 1e) also shows a similar pattern of vertical flows (Figure 1a), although the slanting wall causes the interior and exterior pocket upwellings to merge, which eliminates localized downwelling along the vertical pocket boundary (Figure 1a).

[21] These simulations confirm a general prediction of previous work, which found that under shear, lateral variations in viscosity induce SDU within low-viscosity pockets on their upstream sides [Conrad et al., 2010]. The above examples additionally demonstrate a second region of less intense upwelling occurring outside of the low-viscosity pocket. This outside-pocket upwelling is separated from the interior-pocket upwelling by a downwelling when the pocket wall is nearly vertical. We observe an inverted pattern near downstream walls, which includes a minor upwelling along a nearly vertical wall that separates two regions of downwelling flow (Figure 1a). Other simulations have confirmed these basic patterns for a wide range of lateral viscosity variations, including a variety of shapes and viscosity gradients, although we do not discuss the details those experiments here. In the next section, we examine time-dependent simulations that begin with a rectangular pocket (Figure 1c)

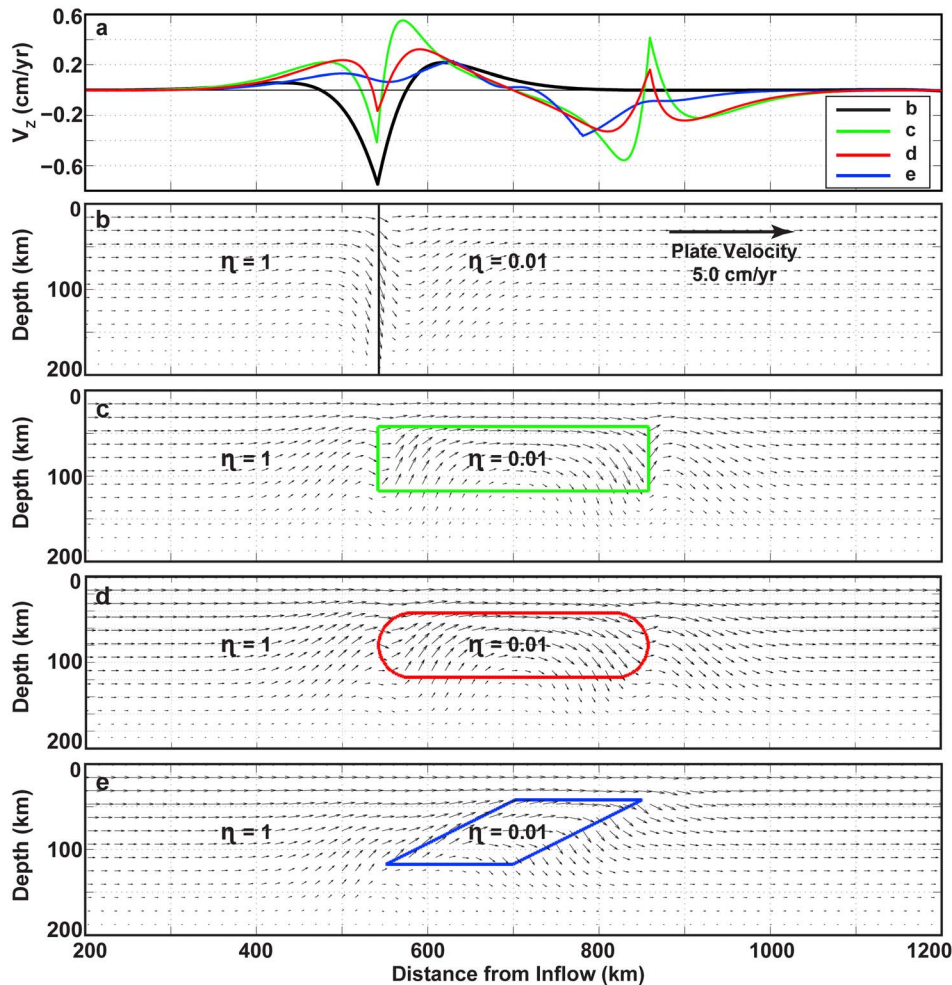


**Figure 1.** (a) Vertical velocity at 80 km depth shown for four different cases of lateral variation (2 orders of magnitude in amplitude) in the asthenosphere: (b) a vertical wall (black line), (c) a rectangular pocket (green line), (d) a pocket with circular walls (red line), (e) a pocket with right-leaning walls. In all cases, plate motion is to the right at 5.0 cm/yr and is zero at the asthenospheric base (200 km depth). In Figures 1b–1e, arrows show the nondimensional velocity in the asthenosphere where the vertical component is exaggerated by a factor of 10. Viscosity drops by 2 orders of magnitude from right to left at 540 km from the inflow boundary. Figures 1c–1e are as in Figure 1b, but a colored contour surrounds the area of the low-viscosity pocket.

and deform with time into shapes similar to the case with right-leaning walls (Figure 1e).

### 3.2. Melting and Eruption Centers

[22] We compute locations and volumes of melt associated with flow driven by asthenospheric shear and asthenospheric viscosity heterogeneity. We express rates of melt eruption onto the surface in terms of the “thickening rate” (in km/Myr), which is the rate at which the basaltic surface layer would thicken if all melt were emplaced uniformly onto the surface above the location of melting. In simulations with a rectangular pocket, there are initially three eruption zones on the surface (i.e., locations with nonzero thickening rate, Figure 2a) above three melting zones in the asthenosphere (Figure 2b). These melting zones occur within the residual mantle layer in the three regions of upwelling described above (Figures 1a and 1c). There is an initially weak

melting zone outside of, and upstream from, the pocket. This “outside” melting zone is distinct from a second region of stronger melting located within the pocket; these two melting zones are separated by the downwelling along the boundary wall (Figure 1a). The third melting zone, at approximately 860 km (Figure 2b), results from upwelling along the downstream pocket wall. Because this melting zone only exists if the pocket boundary is nearly vertical, it is short-lived and we will ignore it in this manuscript.

[23] The lateral spans of the melting zones are controlled by the pattern of vertical velocity in the asthenosphere (Figure 2b), which is dependent on various model parameters such as pocket dimensions and shape. The depth of the top of the melting zones is also controlled by the pattern of vertical velocity; however, this depth is effectively controlled by the exhaustion of clinopyroxene from peridotite [Katz *et al.*, 2003], which decreases productivity ( $\partial F/\partial P$ ).

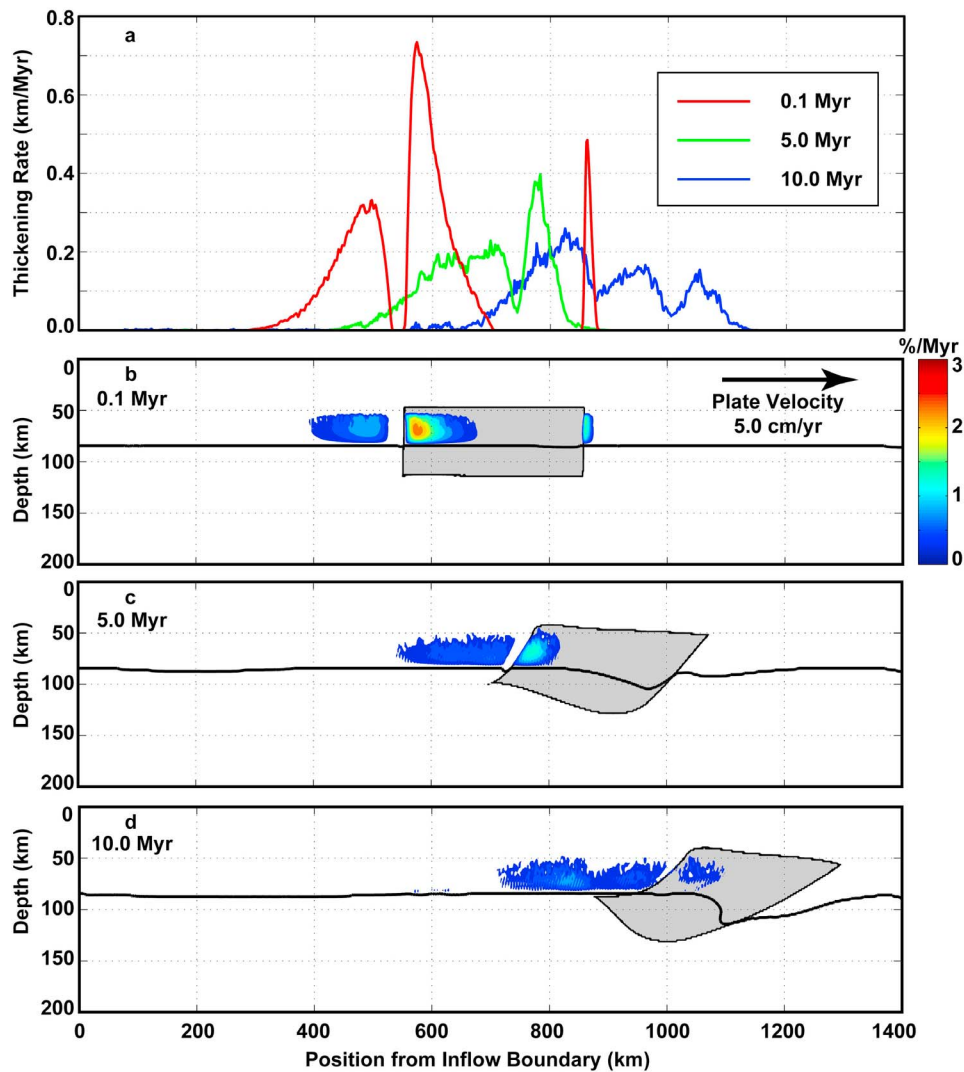


**Figure 2.** (a) The rate of melt emplacement at the surface, or thickening rate, at 0.1 (red line), 5.0 (green line), and 10.0 (blue line) Myr. (b) Model space at 0.1 Myr. The solid line is the base of residual mantle layer, and the shaded region is the low-viscosity pocket, which is 2 orders of magnitude less viscous than the ambient mantle. Color contours are melting rate in %/Myr. (c) As in Figure 2b, but at 5.0 Myr. (d) As in Figure 2b, but for 10.0 Myr.

The depth to the base of the melting zone is controlled by the depth at which the geotherm (typically a mantle adiabat in our simulations) intersects the modeled solidus of peridotite [Katz *et al.*, 2003], which is also the depth of the residual layer at  $t = 0$ . This depth is entirely model dependent, and deepens with increasing potential temperature and water content.

[24] The locations and magnitudes of melting and associated surface eruption change with time as the pocket moves in the direction of plate motion and deforms. For example, after 5 Myr, the eruption center above the pocket (i.e., the location of maximum thickening rate) has moved ~200 km to the right, (Figure 2a) while the plate surface has moved 225 km to the right. Thus, in the reference frame of the moving plate, the eruption center has only moved ~25 km after 5 Myr in a direction opposite to plate motion. The two long-lived melting zones (inside and outside of the pocket) evolve with time in different ways. After 5 Myr, the

vigor of melting inside the pocket has significantly decreased (Figure 2c), diminishing the maximum thickening rate by ~37% above the pocket (Figure 2a). Meanwhile, melting outside of the pocket has decreased only slightly, and its lateral extent has increased. As time progresses, the two eruption zones at the surface begin to coalesce due to tilting of the pocket wall and vertical ascent of magma. After 10 Myr, melting inside the pocket has continued to decrease significantly, while melting outside the pocket persists as it did at 5 Myr (Figure 2d).

### 3.3. Spatial and Temporal Patterns

[25] One interesting aspect of SDU is that melting zones move with plate motion (Figure 2). This movement of the melting zones causes a temporal pattern of eruption that differs from that of a classic hot spot, which forms a line of volcanoes that lengthens at a rate equal to the plate velocity [Wilson, 1963; Morgan, 1971, 1972]. Contours of thickening

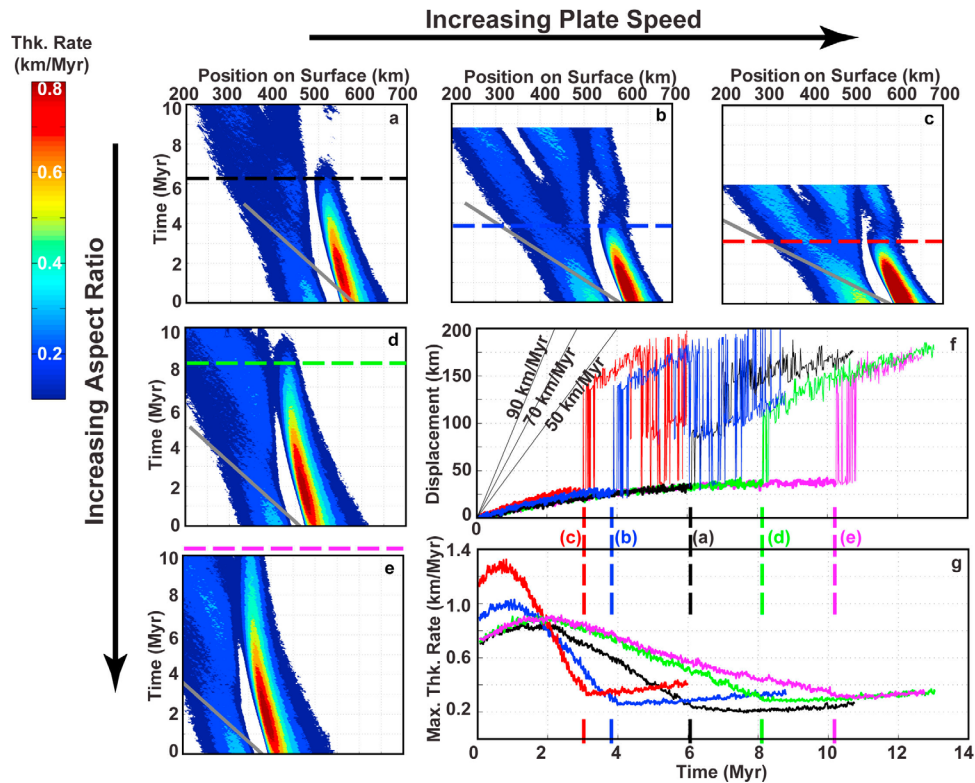


**Figure 3.** (a) Contours of thickening rate (rate of melt emplacement at the surface) as a function of time and surface position (in the reference frame of a position at the surface). Dark shaded line is the track that classic hot spot volcanism would take in this diagram. In Figure 3a, the pocket is 40 km below the surface, has a height of 80 km, and has a length of 320 km (aspect ratio = 4); is centered at about 700 km at 0 Myr; and lies beneath a plate moving at 50 km/Myr. Contours to the right of  $\sim 500$  km show the eruption zone arising from melting within the pocket, while contours to the left show melting outside of the pocket. The dashed line marks our measurement of the time scale for the decrease in within-pocket melting: it is measured as the time at which the maximum thickening rate above the pocket is first equal to the maximum thickening rate beyond the pocket. (b, c) As in Figure 3a, but for plate speeds of 70 km/Myr and 90 km/Myr, respectively. (d, e) As in Figure 3a, but for pocket widths of 480 (aspect ratio = 6) and 640 km (aspect ratio = 8), respectively. (f) The displacement of the location of maximum thickening rate with time, with colored lines corresponding to the colors of the dashed lines in Figures 3a–3e marking the measured time scale. The smooth section of each curve occurs while pocket melting is much stronger than melting outside of the pocket, while the high-amplitude section occurs after pocket melting has diminished (the switchover defines the time scale for pocket melting duration, denoted by dashed lines corresponding by color to Figures 3a–3e). Thin shaded lines in Figure 3f show the expected displacement of a hot spot on plates with different speeds. (g) Maximum thickening rate predicted on the surface versus time, where colors correspond to dashed lines in Figures 3a–3f.

rate on axes of model time versus surface position (an “eruption-gram” that shows patterns of eruption in the reference frame of an observer on the surface) illustrate the differences between the spatial and temporal patterns caused by SDU and a classic hot spot (Figure 3). In this frame, a classic hot spot eruption center plots on a line with a slope equal to  $-1/V_{\text{plate}}$  (shaded lines in Figures 3a–3e). This slope is dramatically steeper than the slope of a line through the maximum melting that arises from SDU volcanism. Specifically, SDU volcanism produces a volcanic age progression that migrates across the Earth’s surface much more slowly than classic hot spot volcanism. For example, in our reference model (Figure 3a), the center of maximum eruption (which results from melting inside the pocket) moves from  $\sim 550$  km to  $\sim 525$  km in 5 Myr. This 25 km displacement is

an order of magnitude smaller than the predicted 250 km displacement of a hot spot center. The eruption center caused by melting outside the pocket also travels about an order of magnitude more slowly compared to a hot spot. The model prediction that SDU melting centers do not result in hot spot-like temporal patterns is not significantly affected by pocket shape or plate velocity (Figures 3a–3e). The location of the maximum thickening rate thus migrates slowly for several million years until the inside-pocket melting diminishes such that the center of maximum volcanism jumps to the more dispersed outside-pocket melting zone (Figure 3f). We note that if the base of the pocket is nearly stationary with respect to the mantle, a more hot spot-like pattern can develop at the surface. For melting to occur in this scenario, however, the

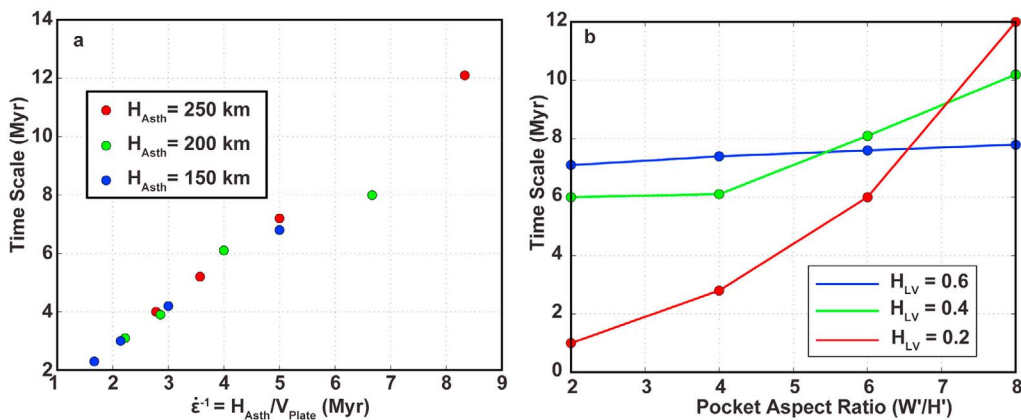


**Figure 4.** Time scale for pocket melting duration as a function of (a) asthenospheric strain rate  $\dot{\epsilon}^{-1} = H_{\text{Asth}}/V_{\text{Plate}}$ , where colors indicate measurements for different asthenosphere thickness, and (b) pocket aspect ratio, where colors indicate different dimensionless pocket heights  $H_{LV}$ .

residual mantle layer must be thicker (e.g., higher  $T_p$ ), or the asthenosphere must be thinner than we have modeled.

[26] Another interesting prediction is that two or more distinct melting centers simultaneously exist, with comparable melt thickening rates at the surface (Figure 2). This pattern is different from that of a classic hot spot, which has a single melting center. Initially, a single melting center occurring within the pocket dominates the surface expression of volcanism: surface thickening above the pocket is stronger than that outside the pocket by more than a factor of five in some cases (Figure 3g). However, as the pocket deforms, melting inside the pocket weakens while melting outside the pocket continues unabated. Eventually, thickening rates above the pocket are indistinguishable from those beyond the pocket edges, and a wide zone of diffuse and weak volcanism results. In all simulations tested there are eventually at least three coexisting eruption zones (e.g.,  $>6$  Myr in Figure 3b), although this time is not shown for all cases. Two or more eruption centers of comparable magnitude can be identified by high-amplitude, high-frequency variations in a plot of location of maximum thickening rate versus time (Figure 3f). The distance between the inside-pocket and outside-pocket eruption centers is typically 100–300 km, and tends to increase with time and plate velocity.

### 3.4. Duration of Melting

[27] Melting caused by SDU does not appear to approach zero during the model time we have examined ( $\sim 10$  Myr). As described above, melting inside the pocket weakens over time and eventually becomes similar to that beyond the pocket edge. To estimate a time scale for the duration of inside-pocket melting, we measure the time at which the maximum thickening location first jumps between these two zones (marked in Figures 3f and 3g), with the understanding that this is not the total duration of melting inside the pocket. We find that the time scale of melting inside the pocket is controlled by the rate of pocket deformation. In particular, we show (Figure 4a) that the time scale increases inversely with the rate of asthenospheric shear ( $\dot{\epsilon} = V_{\text{plate}}/H_{\text{Asth}}$ ) for combinations of  $V_{\text{plate}}$  between 30 to 90 km/Myr and  $H_{\text{Asth}}$  between 150, 200, and 250 km.

[28] Pocket deformation occurs primarily on the edges of the pocket, where the pocket sides become tilted and thinned (Figure 2). Thus, increasing pocket deformation tends to confine the most vigorous circulation toward the center of the pocket, away from the thinned edges. Therefore, for a given pocket height, increasing the pocket aspect ratio (i.e., pocket width) should tend to increase the duration of rapid melting because wider pockets can maintain a central circulation away from the thinned edges for a longer time period. This trend is exactly what we find (Figure 4b). We observe a stronger dependence of melting duration on aspect ratio for short pockets (e.g.,  $H_{LV} = 0.2$ ), primarily because the overlap of the pocket and residual mantle column is comparable to the vertical scale of the circulation pattern. In taller pockets (e.g.,  $H_{LV} = 0.6$ ), much of the weakening in circulation occurs below the residual mantle column, and thus has little effect on melt generation.

### 3.5. Thickening Rates

[29] The instantaneous thickening rate at the surface is dependent on parameters that control how much material near its solidus is decompressing, and on parameters that control the rate of that decompression. In general, the taller melting columns produce greater thickening rates at the surface. Therefore, a pocket positioned deeper beneath the surface has a shorter melting column (i.e., shorter overlap with the residual mantle layer) and a smaller instantaneous thickening rate (Figure 5a). Similarly, increasing the thermal age of the plate (i.e., the thickness of the asthenosphere that has cooled) truncates the top of the melting column, and decreases column height and thus thickening rate (not shown). For example, our simulations predict that half-space cooling at the top of a residual mantle layer will produce a thick enough thermal boundary layer to shut off melting from SDU after only 15 Myr in simulations where there is no initial boundary layer overlying the residual mantle layer (e.g., as in a ridge environment). This estimate of the time before surface cooling shuts off SDU melting (i.e., 15 Myr) is sensitive to model parameters, and will be larger for less refractory mantle material, higher  $T_p$ , diminished thermal diffusivity of the mantle, or the insulating effect of an overlying layer of mechanical lithosphere (i.e., if the

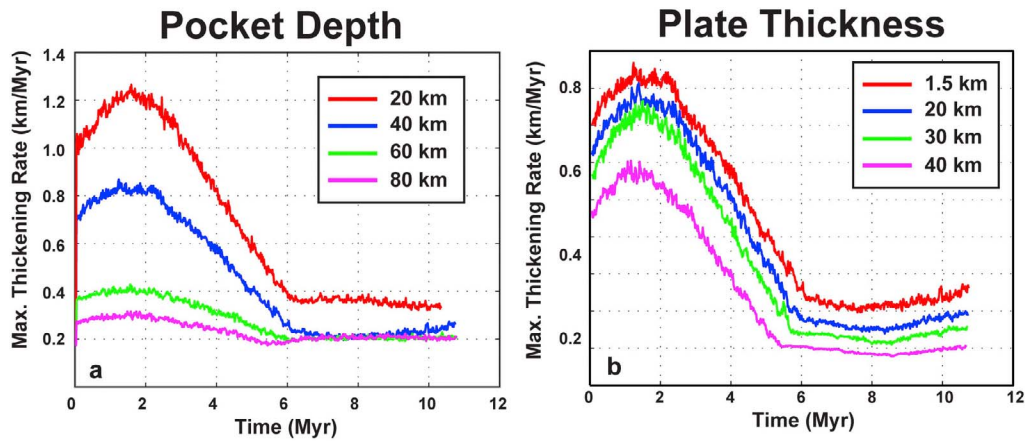


**Figure 5.** Maximum thickening rate at the surface as a function of time for (a) different thicknesses of an overlying mechanical lithosphere and (b) different depths of the pocket below the surface (the mechanical lithosphere is  $\sim 1.5$  km thick in these cases).

residual mantle layer is not initially exposed to the surface). Therefore this prediction should be taken to mean only that SDU cannot cause melting after all of the residual mantle layer has cooled. In the remaining results shown here, we have focused on cases in which there has not been significant cooling beneath a mechanical lithosphere of some thickness (which may represent either continental or oceanic lithosphere).

[30] Many parameters that control the rate of circulation in the pocket have been examined in previous work, and we will not discuss them in detail here [Conrad *et al.*, 2010]. For example, both greater viscosity contrast and surface plate velocity increase vertical velocity, which increases the instantaneous thickening rate (but decreases the duration of melting, as shown above). Increasing the pocket aspect ratio also increases the vertical velocity (or has only a weak affect), and likewise may increase instantaneous thickening rate. As a final example, increasing the mechanical plate thickness decreases pocket circulation and maximum thickening rate (Figure 5b).

[31] Previous work [e.g., Conrad *et al.*, 2010] did not examine the potential for melting outside of the pocket. In that location, upwelling flow is generated by the presence of the pocket viscosity heterogeneity, but does not significantly depend on the pocket's shape. Because the pocket itself persists over time, melting upstream from the pocket is relatively steady and the associated thickening rate at the surface is also relatively steady over the duration of our simulations. Thickening rate upstream from the pocket increases linearly with  $\dot{\epsilon}$  and decreases with the depth of the pocket relative to the surface. Additionally, thickening the mechanical lithosphere inhibits circulation around the top of the pocket, which decreases the thickening rate (see Figure 5b, after  $\sim 6$  Myr).

[32] The cumulative thickening above the pocket is affected by both the duration of melting and the instantaneous thickening rate. For example, the instantaneous thickening rate increases linearly with  $V_{\text{plate}}$ , but the time scale of pocket melting decreases with  $V_{\text{plate}}$ , making the cumulative thickness above the pocket relatively insensitive to  $V_{\text{plate}}$  (Figure 6a). When varying the parameters of plate thickness, pocket aspect ratio, and pocket depth, the predicted time

scale, thickening rate, and consequently cumulative thickening, increase together (Figures 6b–6d). Time scale is not a factor for the steady melting zone outside of the pocket; only thickening rate is important to the cumulative thickness away from the pocket. Thus increasing plate velocity, increasing aspect ratio, decreasing pocket depth, and decreasing the mechanical or thermal lithospheric thickness all tend to increase outside-pocket cumulative thickness. In general, cumulative thickness is most sensitive to the height of the melting column, which is controlled by pocket depth, plate thickness, and plate age in our tests, but also by other factors we have not tested such as, mineralogy,  $T_p$  and other thermodynamic parameters. At 10 Myr, melting outside the pocket produces an erupted thickness between  $\sim 0.5$ – $2.0$  km at the surface, and melting inside the pocket produces a  $\sim 1.0$ – $4.0$  km thick layer.

#### 4. Simulations With Realistic Viscosity Variations

[33] So far, we have induced shear-driven upwelling by simply imposing low viscosities within asthenospheric pockets without considering the source of the asthenospheric heterogeneity that is responsible for the low viscosities. The most likely causes of low-viscosity heterogeneity are regional changes in the water content or temperature of asthenospheric rocks, which can produce larger viscosity variations compared to other factors such as grain size variations and melt retention [see, e.g., Hirth and Kohlstedt, 2003, Table 1]. However, under some conditions, melt retention may cause order-of-magnitude variations in viscosity if high-porosity melt channels form [e.g., Kohlstedt *et al.*, 2010]. While both water and heat can decrease rock viscosity, and therefore can excite SDU in the presence of asthenospheric shear, both also induce changes in the upwelling and/or melting behavior that can affect volumes and patterns of surface volcanism.

##### 4.1. Damp Pockets

[34] We introduce a hydrous source for the 2 orders of magnitude viscosity decrease within the pocket by following the procedure described in section 2.2. For imposed low

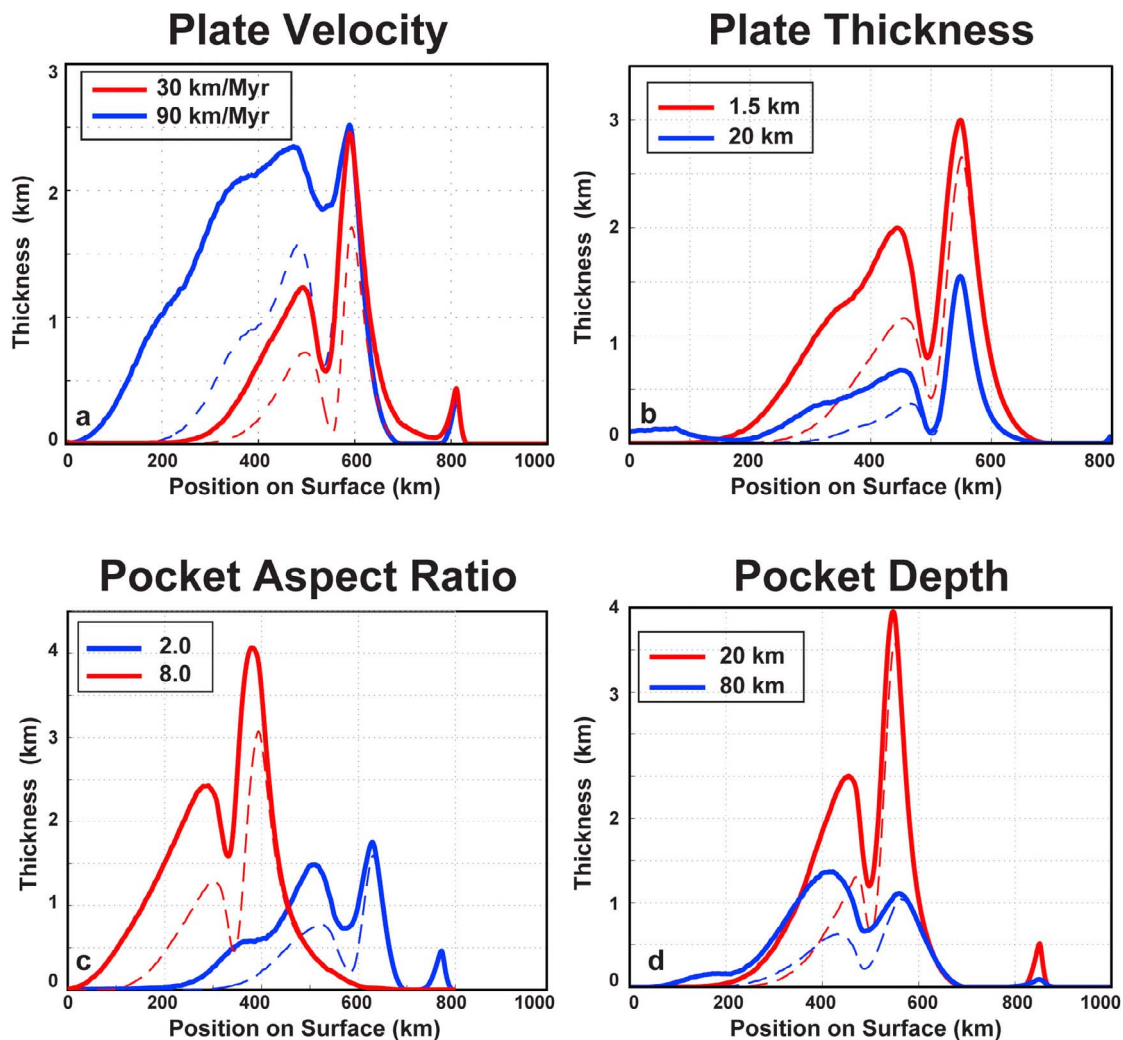


**Figure 6.** Cumulative volcanism at 5 Myr (dashed lines) and 10 Myr (solid lines) as a function of location on the plate for different (a) plate velocities, (b) thicknesses of the mechanical lithosphere, (c) pocket aspect ratios assuming  $H_{LV} = 0.4$ , and (d) depths of the pocket below the surface (the mechanical lithosphere is  $\sim 1.5$  km thick, except in Figure 6b).

viscosities, the duration of melting and the surface eruption pattern are predominantly controlled by asthenospheric strain rates, and, to a lesser extent, the shape and dimensions of the pocket (Figure 4). Water content in the pocket does not significantly affect these parameters, and thus does not greatly influence the duration of volcanism. The rate of melting, however, which is expressed at the surface by thickening rate, is predominantly controlled by the height and productivity of the melting column (Figures 5–6), and these properties are affected by water content.

[35] One might expect that progressive melting inside the damp pocket should dehydrate the peridotite, increase the viscosity or decrease the size of the pocket, and consequently should shorten the measured time scale of melting inside the pocket. However, the simulations predict no significant difference in time scale between imposed and damp pockets. The dynamics modeled here and in the work of Conrad *et al.* [2010] are affected by order-of-magnitude changes in pocket viscosity. Thus, while peridotite that rises, for example, from  $\sim 100$  km depth to  $\sim 90$  km depth in

Figure 7a, does experience dehydration, the accompanying small change in viscosity does not have a large effect on upwelling. On the other hand, moving damp material from  $\sim 140$  km depth to  $\sim 80$  km depth does yield an order-of-magnitude increase in viscosity, and thus should result in stagnating SDU. However, moving this vertical distance, even at the higher end of upwelling rates caused by SDU, requires  $>10$  Myr, or more than double the typical measured time scale. Further, throughout most of the melting zone, the melting rates are  $<0.1\%$ /Myr, while an order-of-magnitude increase in viscosity requires an increase in  $F$  of  $\sim 2\%$ , or roughly 20 Myr. Therefore, the dimensions and shape of a low-viscosity pocket evolve with time rather similarly for damp and imposed pockets over a time scale of  $\sim 10$  Myr.

[36] To exemplify damp pocket melting, we show thickening rate versus position (Figure 7a) for a 320 km wide damp pocket with 400 ppm water in peridotite [e.g., Michael, 1988; Dixon *et al.*, 2002, 2004; Asimow and Langmuir, 2003] that is below a 50 km thick plate (Figure 7b). This damp pocket initially extends from 140 to 50 km depth (the

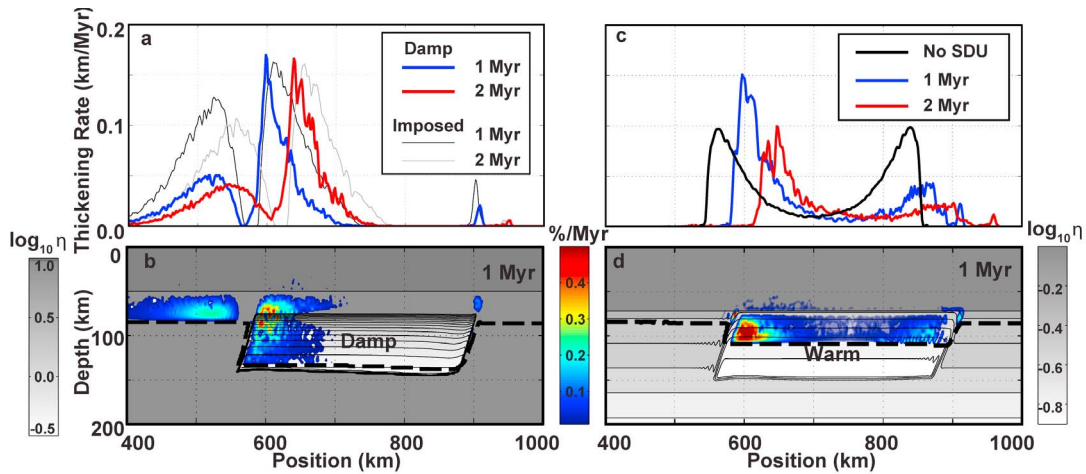


**Figure 7.** (a) The thickening rate over a damp pocket plotted at 1 Myr (blue line) and 2 Myr (red line) for a simulation in which plate velocity is 50 km/Myr and the mechanical plate thickness is 50 km. The pocket peridotite initially contains 400 ppm water, is 320 km wide, and is initially centered at 700 km. The effective pocket height is 70 km, and the effective depth is 70 km. Also shown is the thickening rate for an imposed pocket with the same parameters at 1 Myr (solid line) and 2 Myr (shaded line). (b) Contours show the variation in viscosity (gray scale with thin contour lines) and melting rate (color scale) due to a damp pocket in the asthenosphere at 1 Myr; the pocket is initially rectangular. The bold dashed line indicates the depth of the residual mantle layer. Figure 7b relates to the blue line in Figure 7a. (c) The thickening rate over a warm pocket shown for a simulation in which plate velocity is 0 km/Myr (no shear, solid line) and one in which plate velocity is 50 km/Myr at 1 Myr (blue line) and 2 Myr (red line). In both simulations, the mechanical plate is 70 km thick. (d) As in Figure 7b, but for a warm pocket at 1 Myr. This plot relates to the blue line in Figure 7c.

base of the plate). However, the effective height of this pocket is at most  $\sim 70$  km, because above 70 km depth (i.e., 20 km beneath the plate), melting has depleted hydrous peridotite such that incompatible water [Michael, 1995] has escaped with the magma, leaving behind a residue that is effectively dry. This predicted depth of dehydration is dependent on our choice of mantle conditions, melting model, fractionation model, and bulk partition coefficient of water, and is consistent with the predictions of Hirth and Kohlstedt [1996]. Furthermore, only the deepest  $\sim 25$  km of the remaining pocket experiences a viscosity decrease near 2 orders of magnitude, and the top  $\sim 25$  km experience on average less than 1 order of magnitude decrease. Considering these predictions, the true effective height of the pocket is  $< 70$  km, and the true effective depth is  $> 20$  km beneath the base of the plate. For comparison, we also show the thickening rate above an imposed pocket with a height of 70 km, and that is 20 km beneath a 50 km thick plate (Figure 7a).

[37] The displacement of volcanism after 1 Myr is similar for the damp and imposed pockets, as is the pattern of surface eruption as a function of time (e.g., Figure 3). The thickening rate upstream of the pocket is smaller for the damp pocket, because of weaker circulation around the (effectively) shorter damp pocket. A decrease in thickening rate above the pocket does not occur because of a balance between three competing effects. First, the damp pocket has a taller melting column because water increases the pressure (thus depth) at which peridotite begins melting for a given temperature [e.g., Hirose and Kawamoto, 1995; Gaetani and Grove, 1998; Hirschmann et al., 1999; Katz et al., 2003]. Therefore, the mantle residual layer extends deeper inside the damp pocket

than in the adjacent mantle (Figure 7a), which increases the thickening rate at the surface. Second, a damp pocket may decrease surface thickening rates because water necessarily decreases  $\partial F/\partial p$  (and melting rate) for low  $F$  relative to dry peridotite [e.g., Hirose and Kawamoto, 1995; Gaetani and Grove, 1998; Hirschmann et al., 1999]. Third, we find that vertical velocity is actually smaller throughout the upper half of the damp pocket compared to the imposed pocket, because the effective height of the damp pocket is shorter. In the example simulation, these competing effects approximately cancel, which causes thickening rates above damp and imposed pockets to be similar. In other simulations with greater plate thickness, damp pockets tend to produce more magma than imposed pockets.

[38] Finally, we note that shallow low-viscosity pockets cannot result from excess water unless the damp region is not at equilibrium with the surrounding mantle. This may be the case, for example, if water is brought into the mantle from above near subduction zones [e.g., Stern, 2002]. However, the melting associated with such a pocket would include a component caused by solidus depression of hydrous minerals, which would occur even in the absence of upwelling. Our assumptions isolate the magnitude of decompression melting caused by SDU.

#### 4.2. Warm Pockets

[39] Although warm pockets are less viscous than the ambient mantle, they are also buoyant, which causes them to exhibit different dynamics than both damp and imposed pockets. A warm pocket beneath a stationary plate will thin and spread due to its buoyancy via a “gravity current”

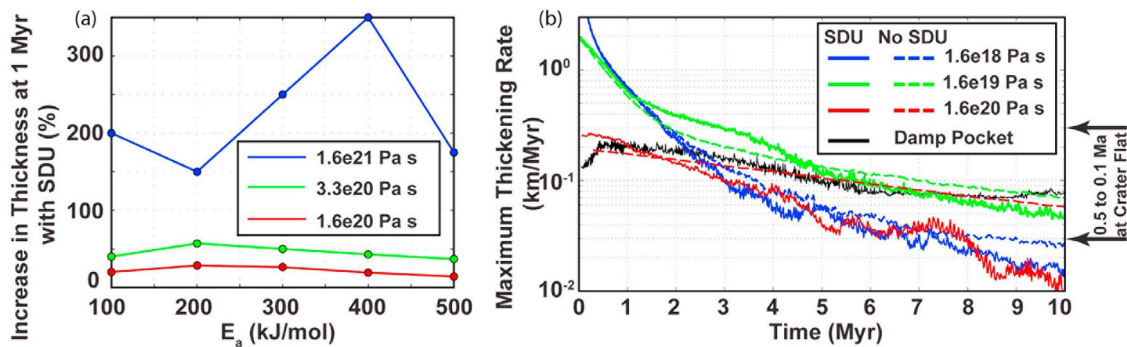


**Figure 8.** (a) The percentage increase in erupted thickness after 1 Myr caused by shear-driven upwelling in a warm pocket beneath a plate moving at 50 km/Myr, relative to the thickness erupted by a warm pocket spreading beneath a stationary plate. Results are plotted as a function of activation energy ( $E_a$ ) for a range of reference viscosities for the asthenosphere (colored lines). (b) Maximum thickening rate versus time for simulations with a warm pocket beneath a stationary plate (dashed colored lines) and beneath a moving plate (solid colored lines). Thickness rate for the damp pocket in Figure 7a is also shown (solid line). Arrows bracket estimates for thickening rates between 0.5 and 0.1 Ma at Crater Flat [Valentine *et al.*, 2006; Conrad *et al.*, 2010].

[Huppert, 1982; Bercovici and Lin, 1996]. The rate of thinning is controlled mostly by the density and viscosity of the pocket, which for warm pockets is determined only by temperature. This thinning can lead to melting because warm material at the base of the pocket is rising and thus depressurizing. To identify the effects of SDU on melting of a warm pocket, we compare the melting patterns of warm pockets spreading beneath a stationary plate to those beneath a plate moving at 5 cm/yr. In our example calculations, we initiate a pocket with a temperature that is 4% greater than the geotherm. The pocket's height is 70 km, width is 320 km, and depth is 70 km. Plate thickness is 70 km,  $\rho_o = 3300 \text{ kg/m}^3$ ,  $\alpha = 4 \times 10^{-5} \text{ K}^{-1}$ ,  $\eta_o = 3.36 \times 10^{20} \text{ Pa s}$ , and  $E_a = 300 \text{ kJ/mol}$ .

[40] The thickening rate above a stationary plate is symmetric about the center of the warm pocket (Figure 7c). Material is rising the fastest at the edges of the pocket where lateral viscosity and density variations are the greatest, and this results in two strong melting centers at the surface that diminish as thinning continues. Unlike patterns predicted for imposed and damp pockets, significant melting does not occur beyond the edges of a warm pocket. In the case of a moving plate, the circulation caused by SDU increases the thickening rate on the upstream side of the pocket, and decreases thickening rate on the downstream side of the pocket (Figure 7c). In our example case, the instantaneous thickening rate is  $\sim 50\%$  greater above the upstream pocket wall, and the total thickness is  $\sim 50\%$  greater after the first million years at this same location.

[41] The extent to which SDU augments melt generation and thickening rate for a warm, buoyant pocket depends on to the amplitude of SDU relative to upwelling induced by thermal buoyancy. For a given set of mantle parameters, such as plate velocity, pocket temperature,  $\rho_o$ ,  $\alpha$ ,  $\kappa$  and height of the model space, the strength of SDU is controlled by the viscosity contrast, which depends on  $E_a$ , whereas the strength of buoyant upwelling is controlled by background viscosity  $\eta_o$ . In our example calculation (Figure 7d) the viscosity contrast results in a maximum SDU velocity that is only  $\sim 1\%$  of the plate velocity. Meanwhile, the density contrast results in a maximum vertical velocity that is  $\sim 6\%$

of plate velocity. Thus melting patterns in this scenario are dominated by buoyant upwelling, and only modified slightly by SDU (Figure 7c).

[42] For all  $\eta_o$  and  $E_a$ , cases with SDU (i.e., moving plates) have thicker crust after  $\sim 1$  Myr (Figure 8a). This extra SDU-induced thickness increases with  $E_a$ , but is insensitive to the order-of-magnitude range of  $\eta_o$  examined here because SDU circulation amplifies with viscosity contrast, rather than with absolute viscosity. However, the background melting caused by buoyant spreading beneath the plate varies by an order of magnitude because it is sensitive to  $\Delta\rho/\eta_o$ . Therefore, the relative amplification of total erupted thickness generated by SDU increases with  $\eta_o$  (Figure 8a). Thus, SDU melting in warm pockets is significant in simulations with  $\eta_o > \sim 10^{20} \text{ Pa s}$ , but insignificant if  $\eta_o < \sim 10^{19} \text{ Pa s}$ . This initial augmentation of melting due to SDU, however, is usually followed by a period of relative suppression of melting after a few million years (Figure 8b), likely because shearing eventually deforms the pocket into a shape that is not conducive to either SDU or efficient spreading.

[43] Given the predictions above, we can assume that there is an optimal set of conditions (e.g., pocket shape,  $\eta_o$ ,  $E_a$ ,  $v_{\text{plate}}$ ) that maximizes the relative importance of SDU for the dynamics and melting of a warm pocket. However, for warm pockets at asthenospheric conditions (e.g.,  $\eta_o \leq \sim 10^{20} \text{ Pa s}$ ), SDU is likely to exert second-order importance.

## 5. Discussion

[44] Our calculations have shown that SDU is a viable process for generating or increasing asthenospheric melting for viscosity heterogeneities that are related to elevated water content, temperature, or other factors. To determine whether SDU melting might actually generate intraplate volcanism on Earth, we compare predictions from our calculations to several observed aspects of intraplate volcanism. Most commonly, intraplate volcanism is classified by eruption rate, duration or age range, spatial and temporal patterns, geochemistry, and the association of the volcanism with geophysical observations such as the presence of a

topographic swell or a thermal anomaly in the mantle [e.g., *Ito and van Keken, 2007*]. With the simulations presented above, we can make comparisons to observed eruption rates, durations, and spatial and temporal patterns. We focus on the damp and warm pockets, which have rheologies based on experimental results.

[45] Examples of intraplate volcanism exist throughout the western United States. Many of these volcanic fields, particularly throughout the Basin and Range and Colorado Plateau, have relatively low eruption volumes and rates, represent short durations, and do not collectively form an obvious hot spot track. For example, the Quaternary Crater Flat volcanic field in southern Nevada is a group of monogenic cones that erupted over 0.1 to 0.5 Myr, with a total volume of  $\sim 0.15\text{--}0.18\text{ km}^3$ , and with a thickening rate roughly estimated as  $\sim 0.03$  to  $0.3\text{ km/Myr}$  [*Valentine et al., 2006; Conrad et al., 2010*]. This particular section of the Basin and Range overlies relatively thin continental lithosphere extending to only 50–70 km depth [*Li et al., 2007*], and a low-viscosity zone of  $\sim 10^{18}\text{ Pa s}$  may exist between  $\sim 80\text{--}160\text{ km}$  depth [*Bills et al., 2007*]. The shear across the asthenosphere beneath Crater flat is estimated between  $\sim 4\text{--}8\text{ cm/yr}$  [*Silver and Holt, 2002; Conrad and Behn, 2010*], and tomography reveals a approximately  $-1.5\%$  anomaly in  $P$ -wave velocity in the asthenosphere just south of Crater Flat, which spans  $\sim 200\text{ km}$  at its widest and is up to  $\sim 200\text{ km}$  tall [*Dueker et al., 2001; Schmandt and Humphreys, 2010; Xue and Allen, 2010*]. These are all favorable conditions for SDU to produce asthenospheric melting. Furthermore, there is some evidence that the low viscosities beneath Nevada can be attributed to high water content [*Dixon et al., 2004; Plank et al., 2008*].

[46] A damp pocket experiencing SDU can explain the rate of volcanism at Crater Flat. For example, the simulation of a damp pocket beneath a 50 km thick plate discussed above (Figure 7) predicts a maximum thickening rate of  $\sim 0.17\text{ km/Myr}$ , when the pocket has a rectangular shape. After deforming a few million years, the thickening rate levels off  $\sim 0.04\text{ km/Myr}$ . In another simulation with a 70 km thick plate (not show), the same pocket beneath (i.e., a 320 km wide pocket with an effective top at  $\sim 50\text{ km}$  and base at 140 km) yields thickening rates between  $\sim 0.02\text{--}0.056\text{ km/Myr}$  over 10 Myr. These predicted rates compare well with the observed estimated rates at Crater Flat of  $0.03\text{--}0.3\text{ km/Myr}$  [*Valentine et al., 2006; Conrad et al., 2010*]. To erupt the upper bound estimate at Crater Flat, our simulations would have to supply 1.7–15 times more magma, which may require the lateral transport of magma over distances of  $<10\text{ km}$ . This source area would be decreased if the mantle potential temperature was warmer than we estimate, or if the productivity of the mantle is greater than we estimate (e.g., if the mantle contained a pyroxenite component within a peridotite matrix) [*Bianco et al., 2011*]. On the other hand, estimated source area must be increased if the pocket dimensions are smaller, particularly if the melting column is shorter, and this is a limit to melt production in other studies [e.g., *Wang et al., 2002*]. Also, the source area must be increased if the shear rate is lower, if the viscosity contrast is lesser, or if the plate or thermal boundary layer is thicker than we have assumed.

[47] Alternatively, a warm pocket might also explain the rate of volcanism at Crater Flat. In either case (with or without

shear) the warm pockets shown in Figure 7 have comparable thickening rates to those of the damp pockets described above, and we estimate that this rate is comparable to observations at Crater Flat. However, the estimated viscosity of the asthenosphere beneath the Basin and Range is  $10^{18}\text{ Pa s}$  [*Bills et al., 2007*], in which case we predict that SDU melting would be negligible for a warm pocket. The example simulations of warm pockets have a temperature anomaly of 65 K, and predict initial thickening rates on the order of  $10\text{ km/Myr}$  if the asthenosphere's viscosity is  $10^{18}\text{ Pa s}$  (Figure 8b), much larger than what is estimated at Crater Flat. Thus, to explain the rates of volcanism observed at Crater Flat by spreading of a warm pocket beneath southern Nevada requires a smaller pocket, a lower thermal anomaly, or some other factor that reduces upwelling rates such as a less optimal pocket shape.

[48] The volcanism at Crater Flat may be part of a larger volcanic field that stretches from the area around Crater Flat to Lunar Crater Volcanic Field, Nevada, a distance of  $\sim 200\text{ km}$  [*Smith et al., 2002*]. This larger field spans an age range of 10.5–0.08 Ma, with peaks in volcanism separated by 1–2 Myr displaying no age progression [e.g., *Smith et al., 2002; Valentine et al., 2006; Valentine and Hirano, 2010*], but with a noted exponential decay in the volumes erupted intermittently with time over the last  $\sim 4.6\text{ Ma}$  in the area near Crater Flat [*Valentine and Perry, 2006, 2007*]. We predict that both damp and warm pockets do not produce a classic hot spot trail of volcanism on the surface. Further, both types of pockets can produce simultaneous volcanic centers separated by 50–200 km (Figure 7) if the pocket dimensions are on the order of 100 km or more; damp pockets by producing inside- and outside-of-the-pocket melting, and warm pockets because the entire pocket is buoyant. Volcanism from both damp and warm pockets decays with time, with volcanism from a warm pocket decaying exponentially.

[49] The record of eruptions between 10.5 and 0.08 Ma from Crater Flat to Lunar Crater may be better explained by a damp pocket experiencing SDU rather than a warm, buoyant pocket. We show the maximum thickening rate for a damp pocket experiencing SDU compared to a range of warm pockets beneath stationary and moving plates in Figure 8b. The maximum thickening rate for the damp pocket is steadier, and gradually decreases during the 10 Myr of model time, which results naturally from the pocket approaching and then deforming away from shapes that are optimal for SDU. By contrast, a warm pocket with  $\eta_o = 1.6 \times 10^{18}$  and  $1.6 \times 10^{19}\text{ Pa s}$  exhibits initially large thickening rates ( $\sim 2\text{ km/Myr}$  or more) followed by decreases of 1–2 orders of magnitude over 10 Myr. Only a warm pocket beneath a stationary plate with  $\eta_o = 1.6 \times 10^{20}\text{ Pa s}$  produces thickening rates that are comparable to those of the damp pocket (Figure 8b) and estimates for Crater Flat, but such high asthenospheric viscosity are unrealistic for the asthenosphere beneath western North America. If we assume a more reasonable asthenospheric viscosity beneath southern Nevada of  $10^{18}\text{--}10^{19}\text{ Pa s}$ , and attribute melting to a warm region beneath the lithosphere, predicted melting rates would be unrealistically high, especially initially.

[50] Some of the limitations of each type of pocket are mitigated if we assume that the seismic anomalies detected throughout the western U.S. are at once damp and warm [*Dixon et al., 2004*]. In this case, we propose that the viscosity of the pocket is greatly decreased by water content,

allowing for SDU. A slightly elevated temperature increases the melting rate, and thus thickening rate, without producing a strong density contrast; even small variations ( $<10^{\circ}\text{C}$ ) may augment melting in damp, circulating pockets. Heterogeneity in water content may be preexisting or related to subduction [e.g., *Cao and Levander, 2010*], and there is indeed geophysical evidence for compositional variation beneath the Western U.S. [e.g., *Dueker et al., 2001; Gilbert et al., 2003*].

[51] The Newer Volcanic Province (NVP) located mainly in Victoria, Australia, represents another intraplate volcanic field with small eruption volumes and no obvious age progression [e.g., *Demidjuk et al., 2007; Gray and McDougall, 2009*]. Most of this volcanism erupted since 5 Ma with a peak at  $\sim 2$  Ma, covers roughly  $15,000\text{ km}^2$ , and erupted thicknesses are up to 160 m but typically closer to 60 m [*Demidjuk et al., 2007*, and reference therein]. Using U-series disequilibria in samples from the NVP, *Demidjuk et al. [2007]* concluded that mantle upwelling velocity may be  $\sim 1.5\text{ cm/yr}$ , significantly slower than the estimated plate velocity of  $6.5\text{ cm/yr}$ , and that melt was generated in the mantle. Although some authors have cited alignment of volcanism centers as evidence for a tectonic control on magmatism [*Lesti et al., 2008*], *Demidjuk et al. [2007]* note that the lack of motion or widening of the NVP through time suggests that melting is related to absolute plate motion. In that case, *Demidjuk et al. [2007]* favored the edge-driven convection model of *King and Anderson [1998]*, with the southern boundary of the Australian craton forming the “edge” and northward motion of the Australian plate trapping the resulting melt along the trailing edge of the continental keel. Given the thickness of the lithosphere underlying the NVP, the conclusion that edge-driven convection could generate melting relied on the evidence of fertile, hydrous mantle beneath Australia [*Griffin et al., 1988; O’Reilly and Griffin, 1988; Stolz and Davies, 1988; Powell et al., 2004*].

[52] Alternatively, melting caused by SDU associated with a damp pocket could provide an explanation for volcanism since 5 Ma in the NVP. Over this time interval, we predict the center of volcanism should move only  $\sim 25\text{ km}$  to the south, and the volcanic province should not widen (Figure 3). Further, the typical thickness of  $\leq 60\text{ m}$  (also reported to be  $<10\text{ m}$  and up to  $160\text{ m}$ ) [e.g., *Johnson et al., 1989; Price et al., 1997; Demidjuk et al., 2007*] observed at the NVP can be generated by a damp pocket similar to the example in Figure 7a at  $\sim 1\text{ Ma}$ , assuming a plate velocity of  $\sim 6.5\text{ cm/yr}$ . The damp pocket in Figure 7a can produce the melt necessary to form a basalt layer that is  $60\text{ m}$  thick in  $\sim 5\text{ Ma}$  even when the pocket shape is inefficient for SDU, and this is the time span over which the NVP has erupted. If the plate were moving at  $6.5\text{ cm/yr}$  as in the case of Australia, or if the mantle were more fusible than we have modeled, the amount of time necessary to erupt  $60\text{ m}$  of crust would shorten. If the plate were thicker, the necessary time would lengthen.

[53] Small seamounts may represent another type of volcanism caused by SDU. There are more than 190,000 edifices on the seafloor with an estimated volume  $<10^3\text{ km}^3$  [*Hillier, 2007*]. Many of these seamounts are not volcanic, and thus cannot be related to melting by SDU, and many others are better explained by a thermal anomaly or other process unrelated to SDU [e.g., *Wilson, 1963; Morgan, 1971,*

*1972; Buck and Parmentier, 1986; McKenzie and Bickle, 1988; Marquart, 2001; Raddick et al., 2002; Hirano et al., 2006; Ballmer et al., 2007*]. There are, however, many seamounts that can be equally well explained by melting in a damp pocket that is experiencing SDU, particularly those formed on young plates where SDU would generate the most magma. Our calculations show that damp pockets beneath thin, young plates ( $<10\text{ km}$  thick) produce a maximum thickening rate of  $\sim 0.3\text{ km/Myr}$  and a sustained thickening rate of  $\sim 0.1\text{ km/Myr}$ . To form a seamount volume of  $10^3\text{ km}^3$  in 1 Myr with these rates, the seamount would have formed from a source area with a  $\sim 32\text{--}56\text{ km}$  radius. Simulations with damp pockets that have dimensions of  $\sim 100\text{ km}$  do predict that SDU can generate a source volume of this size, but efficiently transporting magma  $\sim 30$  to  $50\text{ km}$  beneath such a thin plate may be difficult [*Hieronymus and Bercovici, 2001*]. More voluminous seamounts, and seamounts that form on plates thicker than  $10\text{ km}$  require a larger source radius, and may be better explained by a thermal anomaly, or may require some combination of thermal or chemical heterogeneity to augment SDU melting, as discussed above. Seamounts of  $\sim 10^2\text{ km}^3$  that have erupted in  $\sim 1\text{ Myr}$  require a source radius of only  $\sim 10\text{--}18\text{ km}$ , which is a reasonable source radius for thin plates [*Hieronymus and Bercovici, 2001*].

[54] The overall implication of our study is that SDU can induce the melting necessary to form some of the small, non-hot spot, intraplate volcanism observed on both the continents and seafloor. Larger volcanic fields, such as Iceland or Hawaii, still likely require a thermal explanation. Our simulations predict that small, anomalous volcanism should preferentially form on continental or oceanic areas that lie above rapidly shearing asthenosphere. This prediction was investigated by *Conrad et al. [2011]*, who found a positive correlation between mantle shear and the occurrence of intraplate basaltic volcanism. Shear rate, the shapes and magnitudes of sublithospheric viscosity heterogeneities, and asthenospheric temperature should all exert controls on the formation of anomalous volcanism by SDU.

## 6. Conclusions

[55] Shear in the asthenosphere can excite circulatory flow within a variety of types of viscosity heterogeneities. In the case of low-viscosity pockets embedded in the ambient asthenosphere, the vertical component of this circulation, known as “shear-driven upwelling” (SDU) causes melting if the upwelling occurs within material near its solidus, such as uncooled (i.e., at the ambient  $T_p$ ) material that was emplaced by passive upwelling beneath a mid-ocean ridge. One robust model prediction is that shearing of an “imposed” low-viscosity pocket induces a strong melting zone near the upstream side of the pocket and a broad circulation around the pocket that generates a separate melting zone further upstream, beyond the pocket boundaries. A second robust prediction is that these two melting zones move nearly at the same velocity as plate motion (except in special cases with deep pockets or thin asthenosphere [see also *Anderson, 2010*]), making them nearly stationary on the plate. Thus, SDU-induced volcanism features little or no age progression at the surface, which distinguishes it from volcanism induced by mantle plumes.

[56] For low-viscosity pockets that are initially rectangular, eruption of melt from upstream of the pocket remains relatively steady with time, while eruption of melt generated within the pocket decreases over a time scale of  $\sim 2\text{--}12$  Myr. This time scale decreases with, and is most sensitive to, asthenospheric strain rate  $\dot{\epsilon}$  (i.e.,  $V_{\text{plate}}/H_{\text{Asth}}$ ), but also tends to increase with the aspect ratio of the pocket ( $W_{LV}/H_{LV}$ ). After this time scale is exceeded, eruption rates from both melting zones tend to be weak but steady, continuing for at least another 10 Myr.

[57] The SDU-induced surface eruption rate (i.e., thickening rate) is most sensitive to the height of the melting column, which is controlled by the overlap of upwelling flow and the residual mantle column. Both are sensitive to the thickness of a mechanical plate, thermal boundary layer, and mantle potential temperature. Little to no melting occurs beneath plates that have cooled to a depth near or below the base of the residual mantle layer. Increasing the mechanical thickness of a plate reduces thickening rates, as does increasing the depth of the pocket below the surface. Cumulative erupted melt volume decreases with plate age, thickness, and depth of the pocket, but increases with the pocket aspect ratio. Damp pockets behave similarly to imposed pockets, with the interesting result that water in the peridotite allows damp pockets to melt beneath thicker mechanical lithosphere and thermal boundary layers than imposed pockets. Warm pockets, however, exhibit a very different behavior that is caused by the buoyancy of the warm material. Assuming a reference viscosity of  $\sim 10^{18}\text{--}10^{19}$  Pa  $\cdot$  s, vertical velocity is dominated by buoyant upwelling and the influence of SDU is negligible. Assuming typical asthenospheric viscosity, thickening rates for warm pockets decrease exponentially with time from initially very high rates of volcanism, and thus have a different surface expression, and shorter lifetime, than imposed or damp pockets. This difference can be used to determine which type of heterogeneity, thermal or compositional, causes a particular observation of intraplate volcanism.

[58] Melting that is excited by SDU occurring within damp pockets can explain intraplate volcanism with eruption volumes up to  $10^2$  km<sup>3</sup>/Myr, corresponding to eruption of a 0.1 km thick melt layer every Myr. SDU may produce greater rates of volcanism if the geometry of the viscosity heterogeneity is particularly optimal for generating SDU, melt focusing is particularly efficient, the asthenosphere contains particularly fusible material, or if SDU is augmented by a thermal anomaly. If we assume that heterogeneity in the water content of peridotite is ubiquitous throughout the mantle, this work predicts that intraplate volcanism should preferentially occur on the surface above regions of high asthenospheric shear, such as western North America or eastern Australia, or on the seafloor near rapidly spreading ridges. In this case, SDU may be a globally important mechanism for the generation of low-volume intraplate volcanism. Consequently, global mantle flow, which is believed to control volcanism at plate boundaries, may also exert a control on intraplate volcanism via SDU.

[59] **Acknowledgments.** This work was supported by NSF grants EAR-0855546 (C.P.C.) and EAR-948345 (T.A.B.), the Nevada Agency for Nuclear Projects, and the Clark County Department of Comprehensive

Planning, Nuclear Waste Division. Simulations of time-dependent calculations were advanced through discussions with Maxim Ballmer and Garrett Ito. The manuscript was improved by reviews from Don Anderson and an anonymous reviewer.

## References

- Allègre, C. J. (1982), Chemical geodynamics, *Tectonophysics*, *81*, 109–132, doi:10.1016/0040-1951(82)90125-1.
- Anderson, D. L. (1989), *Theory of the Earth*, 366 pp., Blackwell, Brookline Village, Mass.
- Anderson, D. L. (2010), Hawaii, boundary layers and ambient mantle-geophysical constraints, *J. Petrol.*, *52*, 1547–1577, doi:10.1093/petrology/egq068.
- Asimow, P. D., and C. H. Langmuir (2003), The importance of water to oceanic melting regimes, *Nature*, *421*, 815–820, doi:10.1038/nature01429.
- Asimow, P. W., M. M. Hirschmann, and E. M. Stolper (2001), Calculation of peridotite partial melting from thermodynamics models of minerals and melts, IV. Adiabatic decompression and the compositions and mean properties of mid-ocean ridge basalts, *J. Petrol.*, *42*, 963–998, doi:10.1093/petrology/42.5.963.
- Ballmer, M. D., J. van Hunen, G. Ito, P. J. Tackley, and T. A. Bianco (2007), Non-hotspot volcano chains originating from small-scale sublithospheric convection, *Geophys. Res. Lett.*, *34*, L23310, doi:10.1029/2007GL031636.
- Ballmer, M. D., J. van Hunen, G. Ito, T. A. Bianco, and P. J. Tackley (2009), Intraplate volcanism with complex age-distance patterns: A case for small-scale sublithospheric convection, *Geochem. Geophys. Geosyst.*, *10*, Q06015, doi:10.1029/2009GC002386.
- Bercovici, D., and J. Lin (1996), A gravity current model of cooling mantle plume heads with temperature-dependent buoyancy and viscosity, *J. Geophys. Res.*, *101*, 3291–3309, doi:10.1029/95JB03538.
- Bianco, T. A., G. Ito, J. van Hunen, M. D. Ballmer, and J. J. Mahoney (2008), Geochemical variation at the Hawaiian hotspot caused by upper mantle dynamics and melting of a heterogeneous plume, *Geochem. Geophys. Geosyst.*, *9*, Q11003, doi:10.1029/2008GC002111.
- Bianco, T., G. Ito, J. van Hunen, M. Ballmer, and J. Mahoney (2011), Geochemical variations at intraplate hotspots caused by variable melting of a veined mantle plume, *Geochem. Geophys. Geosyst.*, *12*, Q0AC13, doi:10.1029/2011GC003658.
- Bills, B. G., K. D. Adams, and S. G. Wesnousky (2007), Viscosity structure of the crust and upper mantle in western Nevada from isostatic rebound patterns of the late Pleistocene Lake Lahontan high shoreline, *J. Geophys. Res.*, *112*, B06405, doi:10.1029/2005JB003941.
- Borch, R. S., and H. W. Green II (1989), Deformation of peridotite at high pressure in a new molten salt cell: Comparison of traditional and homologous temperature treatments, *Phys. Earth Planet. Inter.*, *55*, 269–276, doi:10.1016/0031-9201(89)90075-7.
- Buck, W. R., and E. M. Parmentier (1986), Convection beneath young oceanic lithosphere: Implications for thermal structure and gravity, *J. Geophys. Res.*, *91*, 1961–1974, doi:10.1029/JB091iB02p01961.
- Cao, A., and A. Levander (2010), High-resolution transition zone structures of the Gorda Slab beneath the western United States: Implication for deep water subduction, *J. Geophys. Res.*, *115*, B07301, doi:10.1029/2009JB006876.
- Chopra, P. N., and M. S. Paterson (1984), The role of water in the deformation of dunite, *J. Geophys. Res.*, *89*, 7861–7876, doi:10.1029/JB089iB09p07861.
- Christensen, U., and D. A. Yuen (1985), Layered convection induced by phase transitions, *J. Geophys. Res.*, *90*, 10,291–10,300, doi:10.1029/JB090iB12p10291.
- Conrad, C. P., and M. D. Behn (2010), Constraints on lithosphere net rotation and asthenospheric viscosity from global mantle flow models and seismic anisotropy, *Geochem. Geophys. Geosyst.*, *11*, Q05W05, doi:10.1029/2009GC002970.
- Conrad, C. P., B. Wu, E. I. Smith, T. A. Bianco, and A. Tibbetts (2010), Shear-driven upwelling induced by lateral viscosity variations and asthenospheric shear: A mechanism for intraplate volcanism, *Phys. Earth Planet. Inter.*, *178*, 162–175, doi:10.1016/j.pepi.2009.10.001.
- Conrad, C. P., T. A. Bianco, E. I. Smith, and P. Wessel (2011), Patterns of intraplate volcanism controlled by asthenospheric shear, *Nat. Geosci.*, *4*, 317–321, doi:10.1038/ngeo1111.
- Courtilot, V., A. Davaille, J. Besse, and J. Stock (2003), Three distinct types of hotspots in the Earth's mantle, *Earth Planet. Sci. Lett.*, *205*, 295–308, doi:10.1016/S0012-821X(02)01048-8.
- Davies, G. F. (1988), Ocean bathymetry and mantle convection: 1. Large-scale flow and hotspots, *J. Geophys. Res.*, *93*, 10,467–10,480, doi:10.1029/JB093iB09p10467.

- Davis, E. E., and C. R. B. Lister (1974), Fundamentals of ridge crest topography, *Earth Planet. Sci. Lett.*, *21*, 405–413, doi:10.1016/0012-821X(74)90180-0.
- Demidjuk, Z., S. Turner, M. Sandiford, R. George, J. Foden, and M. Etheridge (2007), U-series isotope and geodynamic constraints on mantle melting processes beneath the Newer Volcanic Province in South Australia, *Earth Planet. Sci. Lett.*, *261*, 517–533, doi:10.1016/j.epsl.2007.07.006.
- Dick, H., J. Lin, and H. Schouten (2003), An ultraslow-spreading class of ocean ridge, *Nature*, *426*, 405–412, doi:10.1038/nature02128.
- Dixon, J. E., L. Leist, C. Langmuir, and J.-G. Schilling (2002), Recycled dehydrated lithosphere observed in plume-influenced mid-ocean-ridge basalt, *Nature*, *420*, 385–389, doi:10.1038/nature01215.
- Dixon, J. E., T. H. Dixon, D. R. Bell, and R. Malservisi (2004), Lateral variation in upper mantle viscosity: Role of water, *Earth Planet. Sci. Lett.*, *222*, 451–467, doi:10.1016/j.epsl.2004.03.022.
- Dueker, K., H. Yuan, and B. Zurek (2001), Thick-structured proterozoic lithosphere of the Rocky Mountain region, *GSA Today*, *11*, 4–9, doi:10.1130/1052-5173(2001)011<0004:TSPLIT>2.0.CO;2.
- Elkins-Tanton, L. T. (2007), Continental magmatism, volatile recycling, and a heterogeneous mantle caused by lithospheric gravitational instabilities, *J. Geophys. Res.*, *112*, B03405, doi:10.1029/2005JB004072.
- Gaetani, G. A., and T. L. Grove (1998), The influence of water on melting of mantle peridotite, *Contrib. Mineral. Petrol.*, *131*, 323–346, doi:10.1007/s004100050396.
- Gao, W., S. P. Grand, W. S. Baldrige, D. Wilson, M. West, J. F. Ni, and R. Aster (2004), Upper mantle convection beneath the central Rio Grande rift imaged by *P* and *S* wave tomography, *J. Geophys. Res.*, *109*, B03305, doi:10.1029/2003JB002743.
- Gilbert, H. J., A. F. Sheehan, K. G. Dueker, and P. Molnar (2003), Receiver function in the western United States, with implications for upper mantle structure and dynamics, *J. Geophys. Res.*, *108*(B5), 2229, doi:10.1029/2001JB001194.
- Gray, C. M., and I. McDougall (2009), K-Ar geochronology of basalt petrogenesis, Newer Volcanic Province, Victoria, *Aust. J. Earth Sci.*, *56*, 245–258, doi:10.1080/08120090802547066.
- Griffin, W. L., S. Y. O'Reilly, and A. Stabel (1988), Mantle metasomatism beneath western Victoria, Australia II: Isotope geochemistry of Cr-diopside lherzolites and Al-augite pyroxenites, *Geochim. Cosmochim. Acta*, *52*, 449–459, doi:10.1016/0016-7037(88)90100-7.
- Gurnis, M. (1988), Large-scale mantle convection and the aggregation and dispersal of supercontinents, *Nature*, *332*, 695–699, doi:10.1038/332695a0.
- Hernlund, J. W., P. J. Tackley, and D. J. Stevenson (2008a), Buoyant melting instabilities beneath extending lithosphere: 1. Numerical models, *J. Geophys. Res.*, *113*, B04405, doi:10.1029/2006JB004862.
- Hernlund, J. W., P. J. Tackley, and D. J. Stevenson (2008b), Buoyant melting instabilities beneath extending lithosphere: 2. Linear analysis, *J. Geophys. Res.*, *113*, B04406, doi:10.1029/2006JB004863.
- Hieronimus, C. F., and D. Bercovici (2001), A theoretical model of hotspot volcanism: Control on volcanic spacing and patterns via magma dynamics and lithospheric stresses, *J. Geophys. Res.*, *106*, 683–702, doi:10.1029/2000JB900355.
- Hillier, J. K. (2007), Pacific seamount volcanism in space and time, *Geophys. J. Int.*, *168*, 877–889, doi:10.1111/j.1365-246X.2006.03250.x.
- Hirano, N., et al. (2006), Volcanism in response to plate flexure, *Science*, *313*, 1426–1428, doi:10.1126/science.1128235.
- Hirose, K., and T. Kawamoto (1995), Hydrous partial melting of lherzolite at 1 GPa: The effect of H<sub>2</sub>O on the genesis of basaltic magmas, *Earth Planet. Sci. Lett.*, *133*, 463–473, doi:10.1016/0012-821X(95)00096-U.
- Hirschmann, M., P. D. Asimow, M. S. Ghiorso, and E. M. Stolper (1999), Calculation of peridotite partial melting from thermodynamic models of minerals and melts III. Controls on the isobaric melt production and the effect of water on melt production, *J. Petrol.*, *40*, 831–851, doi:10.1093/ptrology/40.5.831.
- Hirth, G. (2002), Laboratory constraints on the rheology of the upper mantle, *Rev. Mineral. Geochem.*, *51*, 97–120.
- Hirth, G., and D. L. Kohlstedt (1996), Water in the oceanic upper mantle: Implications for rheology, melt extraction and the evolution of the lithosphere, *Earth Planet. Sci. Lett.*, *144*, 93–108, doi:10.1016/0012-821X(96)00154-9.
- Hirth, G., and D. L. Kohlstedt (2003), Rheology of the upper mantle and the mantle wedge: A view from the experimentalists, in *Inside the Subduction Factory*, *Geophys. Monogr. Ser.*, vol. 138, edited by J. Eiler, pp. 83–105, AGU, Washington, D. C.
- Hofmann, A. W. (1997), Mantle geochemistry: The message from oceanic volcanism, *Nature*, *385*, 219–229, doi:10.1038/385219a0.
- Holtzman, B. K., D. L. Kohlstedt, M. E. Zimmerman, F. Heidelback, T. Hiraga, and J. Hustoft (2003), Melt segregation and strain partitioning: Implications for seismic anisotropy and mantle flow, *Science*, *301*, 1227–1230, doi:10.1126/science.1087132.
- Huppert, H. E. (1982), The propagation of two-dimensional and axisymmetric viscous gravity currents over a rigid horizontal surface, *J. Fluid Mech.*, *121*, 43–58, doi:10.1017/S0022112082001797.
- Ito, G., and P. E. van Keken (2007), Hot spots and melting anomalies, in *Mantle Dynamics, Treatise Geophys.*, vol. 7, edited by D. Bercovici, pp. 371–435, Elsevier, New York.
- Johnson, R. W., J. Knutson, and S. R. Taylor (1989), *Intraplate Volcanism in Eastern Australia and New Zealand*, Cambridge Univ. Press, Cambridge, U. K.
- Jung, H., and S.-I. Karato (2001), Water-induced fabric transitions in olivine, *Science*, *293*, 1460–1463, doi:10.1126/science.1062235.
- Karato, S.-I., M. S. Paterson, and J. Fitzgerald (1986), Rheology of synthetic olivine aggregates: Influence on grain size and water, *J. Geophys. Res.*, *91*, 8151–8176, doi:10.1029/JB091iB08p08151.
- Katz, R. F., M. Spiegelman, and C. H. Langmuir (2003), A new parameterization of hydrous mantle melting, *Geochem. Geophys. Geosyst.*, *4*(9), 1073, doi:10.1029/2002GC000433.
- Kawakatsu, H., P. Kumar, Y. Takei, M. Shinohara, T. Kanazawa, E. Araki, and K. Suyehiro (2009), Seismic evidence for sharp lithosphere–asthenosphere boundaries of oceanic plates, *Science*, *324*, 499–502, doi:10.1126/science.1169499.
- King, S. D., and D. L. Anderson (1998), Edge-driven convection, *Earth Planet. Sci. Lett.*, *160*, 289–296, doi:10.1016/S0012-821X(98)00089-2.
- King, S. D., and J. Ritsema (2000), African hot spot volcanism: Small-scale convection in the upper mantle beneath cratons, *Science*, *290*, 1137–1140, doi:10.1126/science.290.5494.1137.
- Kohlstedt, D. L., and B. K. Holtzman (2009), Shearing melt out of the Earth: An experimentalist's perspective on the influence of deformation on melt extraction, *Annu. Rev. Earth Planet. Sci.*, *37*, 561–593, doi:10.1146/annurev.earth.031208.100104.
- Kohlstedt, D. L., M. E. Zimmerman, and S. J. Mackwell (2010), Stress-driven melt segregation in partially molten feldspathic rocks, *J. Petrol.*, *51*, 9–19, doi:10.1093/ptrology/egp043.
- Langmuir, C. H., E. M. Klein, and T. Plank (1992), Petrological systematics of mid-ocean ridge basalts: Constraints on melt generation beneath ocean ridges, in *Mantle Flow and Melt Generation at Mid-ocean Ridges*, *Geophys. Monogr. Ser.*, vol. 71, edited by J. Phipps Morgan, D. K. Blackman, and J. M. Sinton, pp. 183–280, AGU, Washington, D. C.
- Lee, C.-T., P. Luffi, T. Plank, H. Dalton, and W. P. Leeman (2009), Constraints on the depth and temperatures of basaltic magma generation on Earth and other terrestrial planets using new thermobarometers for mafic magmas, *Earth Planet. Sci. Lett.*, *279*, 20–33, doi:10.1016/j.epsl.2008.12.020.
- Lesti, C., G. Giordano, F. Salvini, and R. Cas (2008), Volcano tectonic setting of the intraplate, Pliocene-Holocene, Newer Volcanic Province (southeast Australia): Role of crustal fracture zones, *J. Geophys. Res.*, *113*, B07407, doi:10.1029/2007JB005110.
- Li, X., X. Yuan, and R. Kind (2007), The lithosphere asthenosphere boundary beneath the western United States, *Geophys. J. Int.*, *170*, 700–710, doi:10.1111/j.1365-246X.2007.03428.x.
- Marquart, G. (2001), On the geometry of mantle flow beneath drifting lithospheric plates, *Geophys. J. Int.*, *144*, 356–372, doi:10.1046/j.0956-540X.2000.01325.x.
- McKenzie, D., and M. J. Bickle (1988), The volume and composition of melt generated by extension of the lithosphere, *J. Petrol.*, *29*, 625–679.
- Mei, S., and D. Kohlstedt (2000), Influence of water on deformation of olivine aggregates: 2. Dislocation creep regime, *J. Geophys. Res.*, *105*, 21,457–21,469, doi:10.1029/2000JB900179.
- Michael, P. (1988), The concentration, behavior and storage of H<sub>2</sub>O in the suboceanic upper mantle: Implications for mantle metasomatism, *Geochim. Cosmochim. Acta*, *52*, 555–566, doi:10.1016/0016-7037(88)90110-X.
- Michael, P. (1995), Regionally distinctive sources of depleted MORB: Evidence from trace elements and H<sub>2</sub>O, *Earth Planet. Sci. Lett.*, *131*, 301–320, doi:10.1016/0012-821X(95)00023-6.
- Moresi, L., and M. Gurnis (1996), Constraints on the lateral strength of slabs from three-dimensional dynamic flow models, *Earth Planet. Sci. Lett.*, *138*, 15–28, doi:10.1016/0012-821X(95)00221-W.
- Morgan, W. J. (1971), Convection plumes in the lower mantle, *Nature*, *230*, 42–43, doi:10.1038/230042a0.
- Morgan, W. J. (1972), Deep mantle convection plumes and plate motions, *Am. Assoc. Pet. Geol. Bull.*, *56*, 203–213.
- Olson, P., and I. S. Nam (1986), Formation of seafloor swells by mantle plumes, *J. Geophys. Res.*, *91*, 7181–7191, doi:10.1029/JB091iB07p07181.
- O'Reilly, S. Y., and W. L. Griffin (1988), Mantle metasomatism beneath western Victoria, Australia I: Metasomatic processes in Cr diopside lher-

- zolites, *Geochim. Cosmochim. Acta*, 52, 433–447, doi:10.1016/0016-7037(88)90099-3.
- Plank, T., A. Tibbetts, E. I. Smith, E. Hauri, C. Lee, and D. Forsyth (2008), Constraints from magmas on the upper mantle beneath the western US, *Eos Trans. AGU*, 89(53), Fall Meet. Suppl., Abstract U53C-08.
- Powell, W., M. Zhang, S. Y. O'Reilly, and M. Tiepolo (2004), Mantle amphibole trace-element and isotopic signatures trace metasomatic episodes in lithospheric mantle, western Victoria, Australia, *Lithos*, 75, 141–171, doi:10.1016/j.lithos.2003.12.017.
- Presnall, D. C., G. H. Gudfinnsson, and M. J. Walter (2002), Generation of mid-ocean ridge basalts at pressures from 1 to 7 GPa, *Geochim. Cosmochim. Acta*, 66, 2073–2090, doi:10.1016/S0016-7037(02)00890-6.
- Price, R. C., C. M. Gray, and F. A. Frey (1997), Strontium isotopic and trace element heterogeneity in the plains basalts of the Newer Volcanic Province, Victoria, Australia, *Geochim. Cosmochim. Acta*, 61, 171–192, doi:10.1016/S0016-7037(96)00318-3.
- Putirka, K. D. (2005), Mantle potential temperatures at Hawaii, Iceland, and the mid-ocean ridge system, as inferred from olivine phenocrysts: Evidence for thermally driven mantle plumes, *Geochem. Geophys. Geosyst.*, 6, Q05L08, doi:10.1029/2005GC000915.
- Raddick, M. J., E. M. Parmentier, and D. S. Scheirer (2002), Buoyant decompression melting: A possible mechanism for intraplate melting, *J. Geophys. Res.*, 107(B10), 2228, doi:10.1029/2001JB000617.
- Ribe, N. M., and U. R. Christensen (1999), The dynamical origin of Hawaiian volcanism, *Earth Planet. Sci. Lett.*, 171, 517–531, doi:10.1016/S0012-821X(99)00179-X.
- Richards, M. A., R. A. Duncan, and V. E. Courtillot (1989), Flood basalts and hotspot tracks: Plume heads and tails, *Science*, 246, 103–107, doi:10.1126/science.246.4926.103.
- Sandwell, D. T., E. L. Winterer, J. Mammerickx, R. A. Duncan, M. A. Lynch, D. A. Levitt, and C. L. Johnson (1995), Evidence for diffuse extension of the Pacific plate from Pukapuka ridges and cross-grain gravity lineations, *J. Geophys. Res.*, 100, 15,087–15,100, doi:10.1029/95JB00156.
- Schmandt, B., and E. Humphreys (2010), Complex subduction and small-scale convection revealed by body-wave tomography of the western United States upper mantle, *Earth Planet. Sci. Lett.*, 297, 435–445, doi:10.1016/j.epsl.2010.06.047.
- Silver, P. G., and W. E. Holt (2002), The mantle flow beneath western North America, *Science*, 295, 1054–1057, doi:10.1126/science.1066878.
- Sleep, N. H. (1990), Hotspots and mantle plumes: Some phenomenology, *J. Geophys. Res.*, 95, 6715–6736, doi:10.1029/JB095iB05p06715.
- Smith, E. I., D. Keenan, and T. Plank (2002), Episodic volcanism and hot mantle: Implications for volcanic hazard studies at the proposed nuclear waste repository at Yucca Mountain, Nevada, *GSA Today*, 12, 4–10, doi:10.1130/1052-5173(2002)012<0004:EVAHMI>2.0.CO;2.
- Stern, R. J. (2002), Subduction zones, *Rev. Geophys.*, 40(4), 1012, doi:10.1029/2001RG000108.
- Stolz, A. J., and G. R. Davies (1988), Chemical and isotopic evidence from spinel ilmenite xenoliths for episodic metasomatism of the upper mantle beneath southeastern Australia, *J. Petrol.*, special volume, 303–330.
- Till, C. B., L. T. Elkins-Tanton, and K. M. Fischer (2010), A mechanism for low-extent melts at the lithosphere-asthenosphere boundary, *Geochem. Geophys. Geosyst.*, 11, Q10015, doi:10.1029/2010GC003234.
- Turcotte, D. L., and E. R. Oxburgh (1978), Intra-plate volcanism, *Philos. Trans. R. Soc. London A*, 288, 561–579, doi:10.1098/rsta.1978.0034.
- Valentine, G. A., and N. Hirano (2010), Mechanisms of low-flux intraplate volcanic fields—Basin and Range (North America) and northwest Pacific Ocean, *Geology*, 38, 55–58, doi:10.1130/G30427.1.
- Valentine, G. A., and F. Perry (2006), Decreasing magmatic footprints of individual volcanoes in a waning basaltic field, *Geophys. Res. Lett.*, 33, L14305, doi:10.1029/2006GL026743.
- Valentine, G. A., and F. Perry (2007), Tectonically controlled, time-predictable basaltic volcanism from a lithospheric source (central Basin and Range Province, USA), *Earth Planet. Sci. Lett.*, 261, 201–216, doi:10.1016/j.epsl.2007.06.029.
- Valentine, G. A., F. Perry, D. Krier, G. Keating, R. Kelley, and A. Cogbill (2006), Small-volume basaltic volcanoes: Eruptive products and processes, and post-eruptive geomorphic evolution in Crater Flat (Pleistocene), southern Nevada, *Geol. Soc. Am. Bull.*, 118, 1313–1330, doi:10.1130/B25956.1.
- van Hunen, J., S. Zhong, N. M. Shapiro, and M. H. Ritzwoller (2005), New evidence for dislocation creep from 3-D geodynamic modeling of the Pacific upper mantle structure, *Earth Planet. Sci. Lett.*, 238, 146–155, doi:10.1016/j.epsl.2005.07.006.
- Wang, K., T. Plank, J. D. Walker, and E. I. Smith (2002), A mantle melting profile across the Basin and Range, SW USA, *J. Geophys. Res.*, 107(B1), 2017, doi:10.1029/2001JB000209.
- West, M., J. Ni, W. S. Baldrige, D. Wilson, R. Aster, W. Gao, and S. Grand (2004), Crust and upper mantle shear wave structure of the southwest United States: Implications for rifting and support for high elevation, *J. Geophys. Res.*, 109, B03309, doi:10.1029/2003JB002575.
- White, R. S., D. McKenzie, and R. K. O'Nions (1992), Oceanic crustal thickness from seismic measurements and rare earth element inversions, *J. Geophys. Res.*, 97, 19,683–19,715, doi:10.1029/92JB01749.
- Whitehead, J., Jr., and D. Luther (1975), Dynamics of laboratory diapir and plume models, *J. Geophys. Res.*, 80, 705–717, doi:10.1029/JB080i005p00705.
- Wilson, J. T. (1963), A possible origin of the Hawaiian Islands, *Can. J. Phys.*, 41, 863–870, doi:10.1139/p63-094.
- Xue, M., and R. M. Allen (2010), Mantle structure beneath the western United States and its implications for convection processes, *J. Geophys. Res.*, 115, B07303, doi:10.1029/2008JB006079.
- Zhong, S., and A. B. Watts (2002), Constraints on the dynamics of mantle plumes from uplift of the Hawaiian Islands, *Earth Planet. Sci. Lett.*, 203, 105–116, doi:10.1016/S0012-821X(02)00845-2.
- Zhong, S., M. T. Zuber, L. Moresi, and M. Gurnis (2000), Role of temperature-dependent viscosity and surface plates in spherical shell models of mantle convection, *J. Geophys. Res.*, 105, 11,063–11,082, doi:10.1029/2000JB900003.
- Zindler, A., and S. R. Hart (1986), Chemical geodynamics, *Annu. Rev. Earth Planet. Sci.*, 14, 493–571, doi:10.1146/annurev.ea.14.050186.002425.

T. A. Bianco, Department of Geological Sciences, Brown University, Providence, RI 02912, USA. (bianco@brown.edu)

C. P. Conrad, Department of Geology and Geophysics, University of Hawaii at Manoa, Honolulu, HI 96822, USA.

E. I. Smith, Department of Geoscience, University of Nevada, Las Vegas, NV 89154, USA.